The Astrophysical Journal, 625:522–538, 2005 May 20

MODELING THE SUN'S MAGNETIC FIELD AND IRRADIANCE SINCE 1713

Y.-M. Wang, J. L. Lean, and N. R. Sheeley, Jr.
Code 7670, E. O. Hulburt Center for Space Research, Naval Research Laboratory, Washington, DC 20375-5352;
ywang@yucca.nrl.navy.mil, jlean@ssd5.nrl.navy.mil, sheeley@spruce.nrl.navy.mil
Received 2004 December 10; accepted 2005 February 15

ABSTRACT

We use a flux transport model to simulate the evolution of the Sun's total and open magnetic flux over the last 26 solar cycles (1713–1996). Polar field reversals are maintained by varying the meridional flow speed between 11 and 20 m s^{-1}, with the poleward-directed surface flow being slower during low-amplitude cycles. If the strengths of the active regions are fixed but their numbers are taken to be proportional to the cycle amplitude, the open flux is found to scale approximately as the square root of the cycle amplitude. However, the scaling becomes linear if the number of active regions per cycle is fixed but their average strength is taken to be proportional to the cycle amplitude. Even with the inclusion of a secularly varying ephemeral region background, the increase in the total photospheric flux between the Maunder minimum and the end of solar cycle 21 is at most ~one-third of its minimum-to-maximum variation during the latter cycle. The simulations are compared with geomagnetic activity and cosmogenic isotope records and are used to derive a new reconstruction of total solar irradiance (TSI). The increase in cycle-averaged TSI since the Maunder minimum is estimated to be ~1 W m^{-2}. Because the diffusive decay rate accelerates as the average spacing between active regions decreases, the photospheric magnetic flux and facular brightness grow more slowly than the sunspot number and TSI saturates during the highest amplitude cycles.

Subject headings: interplanetary medium — solar-terrestrial relations — Sun: activity — Sun: magnetic fields — Sun: photosphere

1. INTRODUCTION

The Sun's external magnetic field consists of two components, one emerging in the sunspot latitudes in the form of large bipoles or active regions, the other emerging everywhere in the form of small bipoles or ephemeral regions. The ephemeral region fields are very short-lived and essentially represent a small-scale background noise (see, e.g., Schrijver et al. 1998). Depending on their estimated rates of emergence, ephemeral regions may provide a major contribution to or even dominate the total photospheric magnetic flux. However, because the axial orientations of bipoles tend to become increasingly random with decreasing size (Howard 1989; Wang & Sheeley 1989; Harvey-Angle 1993; Hagenaar 2001; Hagenaar et al. 2003), the contribution of ephemeral regions to the Sun's net dipole moment is likely to be small (Wang & Sheeley 1991; Harvey 1994). In contrast, the active region component is less well mixed, shows a systematic polarity orientation, and gives rise to an organized large-scale field as it is dispersed over the solar surface. The so-called quiet magnetic network consists of both ephemeral region fields and decayed active region flux.

The large-scale field can in turn be divided into an open and a closed component. Most of the magnetic flux is in the form of closed loops with both footpoints anchored in the Sun; this closed component includes the bulk of the dark sunspots and bright faculae, whose mutual competition leads to variations in the total irradiance (see, e.g., Foukal & Lean 1988). However, because the magnetic field strength falls off rapidly with height, the highest coronal loops—those extending out to heliocentric distances $\gtrsim 2.5\ R_\odot$—are dragged outward by the coronal gas pressure to form the interplanetary magnetic field (IMF) and solar wind.

Although the open magnetic flux constitutes only a small fraction of the total photospheric flux, it plays a major role in controlling geomagnetic activity (Lockwood et al. 1999) and the flux of cosmic rays at Earth (Cane et al. 1999). At least on timescales on the order of or less than a solar cycle, the open flux is rather poorly correlated with sunspot activity, unlike the closed flux that controls the solar irradiance (see Wang et al. 2000). These differences need to be taken into account when using cosmogenic isotope or geomagnetic activity records to infer changes in solar irradiance (Lockwood 2001; Lean et al. 2002).

The basic reason why the variation of the total photospheric flux differs from that of the open flux is that the closed flux is dominated by high-order magnetic multipoles, whereas the open flux is dominated by low-order multipoles. The high-order multipoles are short-lived and have to be continually regenerated by new flux emergence, and as a result the total photospheric flux is closely correlated with sunspot activity. On the other hand, the variation of the open flux follows that of the Sun's total dipole strength, whose two components behave in quite different ways. The axial dipole component ($l = 1$, $m = 0$) varies in a manner similar to the Sun's polar fields, attaining its maximum strength near sunspot minimum and going through zero near sunspot maximum. The equatorial dipole component ($l = 1$, $|m| = 1$) varies roughly in phase with sunspot activity. Corresponding to the two components of the dipole, the open flux consists of a high-latitude component that attains its maximum strength at sunspot minimum and a low-latitude component that varies roughly in phase with sunspot activity. The high-latitude component is dominated by the large, axisymmetric polar coronal holes, whereas the low-latitude component consists mainly of small open-field regions located near active regions and characterized by strong footpoint fields. Unless maintained by new flux emergence, the equatorial dipole and nonaxisymmetric open flux decay on the ~1–2 yr timescale of the surface meridional flow: what happens is that the flow carries the active region remnants to midlatitudes, where differential rotation and supergranular diffusion combine to annihilate the nonaxisymmetric component of the

large-scale field. In contrast, the axial dipole and axisymmetric open flux are unaffected by rotational shearing and survive until the next sunspot cycle, when active regions emerge with the opposite north-south polarity orientation.

Based on the secular increase in geomagnetic activity from 1900 to 1960 and on the empirical correlation between the *aa* index and the IMF strength during 1964–1995, Lockwood et al. (1999) deduced that the Sun's open magnetic flux doubled during the twentieth century. However, this result has been questioned by Svalgaard et al. (2004), who recalibrated the pre-1957 *aa* index and found a much smaller long-term trend.

Solanki et al. (2002) have presented a model for the evolution of the Sun's total and open magnetic flux since 1700. Their reconstruction relies on a number of arbitrary time constants representing the decay of closed active region fields, the conversion of closed active region fields into open flux, the decay of open flux, and the conversion of ephemeral region fields into open flux. The actual transport of flux over the solar surface is not described, and no distinction is made between the behavior of the axisymmetric and nonaxisymmetric field components. By assuming that ephemeral regions provide the dominant contribution to the photospheric flux and that they emerge in overlapping cycles whose amplitudes reflect those of the corresponding sunspot cycles, Solanki et al. (2002) obtained a large secular trend in the total flux, with the cycle minimum values since 1700 increasing by an amount comparable to the present-day minimum-to-maximum variation.

In Wang et al. (2002a), we used a different approach to model the evolution of the Sun's large-scale field during solar cycles 13–22. Our simulations included the effect of emerging flux and its subsequent transport over the solar surface by differential rotation, supergranular convection, and a poleward bulk flow. The source term for each cycle consisted of a collection of 3000 magnetic bipoles, whose locations, orientations, pole separations, and relative strengths were derived from cycle 21 measurements (see Wang & Sheeley 1989) but whose absolute strengths were scaled according to the amplitude of the given cycle. When the meridional flow speed was held fixed, we found that the polar fields built up during the more active cycles were too strong to be reversed during the less active ones (a similar problem was encountered by Schrijver et al. 2002). However, regular polarity oscillations were obtained if the flow rate was taken to be positively correlated with the cycle amplitude. Moreover, the total open flux doubled over the 100 yr interval, in agreement with the empirical reconstruction of Lockwood et al. (1999).

In a subsequent study (Wang & Sheeley 2003b), we constructed a scenario for the evolution of the large-scale field during the 1645–1715 Maunder minimum, when the rate of active region emergence was ~30 times lower than in solar cycle 21 (see Eddy 1976; Hoyt & Schatten 1996). Polarity reversals were maintained by reducing the poleward flow speed from ~20 to $\lesssim$10 m s^{-1} and requiring the flux to emerge at very low latitudes; both of these factors acted to promote the diffusion of leading-polarity flux across the equator and hence to maximize the net amount of trailing-polarity flux reaching the poles. The large-scale field was then found to be ~5–10 times weaker than in the present day.

In this paper, we model the evolution of the Sun's magnetic field and irradiance from the end of the Maunder minimum to the present. As in Wang et al. (2002a) and Wang & Sheeley (2003b), polar field reversals are maintained by allowing the meridional flow speed to vary from cycle to cycle. However, we now take the flux emergence rate to be proportional to the observed yearly sunspot numbers, rather than scaling a generic activity profile (based on cycle 21) upward or downward according to the cycle amplitude. After deriving the evolution of the large-scale field in §§ 2 and 3, we discuss the contribution of ephemeral regions to the total photospheric flux (§ 4), compare the calculated open flux with geomagnetic and cosmogenic isotope records (§ 5), and reconstruct the solar irradiance variation since 1713 (§ 6). Our results and conclusions are summarized in § 7.

2. PROCEDURE FOR MODELING THE LARGE-SCALE FIELD

The flux transport model describes the evolution of the photospheric field when the initial field distribution and the subsequent sources of emerging flux are prescribed (see Sheeley et al. 1985). Let r denote heliocentric distance, L heliographic latitude, ϕ Carrington longitude, and t time. The radially oriented photospheric field $B_r(R_\odot, L, \phi, t)$ is assumed to obey the equation

$$\frac{\partial B_r}{\partial t} = -\,\omega(L)\frac{\partial B_r}{\partial \phi} + \kappa\nabla_\perp^2 B_r - \frac{1}{R_\odot \cos L}\frac{\partial}{\partial L}\left[v(L)B_r \cos L\right] + S(L, \phi, t), \quad (1)$$

where $\nabla_\perp^2$ represents the L and ϕ components of the Laplacian, $\omega(L) = 13.38 - 2.30 \sin^2 L - 1.62 \sin^4 L$ deg day^{-1} is the synodic rotation rate of the photospheric plasma (Snodgrass 1983), κ is the diffusion coefficient associated with the nonstationary supergranular convection (Leighton 1964), $v(L)$ is the meridional flow velocity, and $S(L, \phi, t)$ is the source term. As shown in Wang et al. (2002b), the observed variation of the polar fields and radial IMF component during solar cycle 21 (1977–1986) can be reproduced by taking $\kappa = 500$ km^2 s^{-1} and setting

$$|v(L)| = v_m \cos^2 L \sin^{0.025}|L|, \quad (2)$$

with $v_m \sim 20$ m s^{-1}. The surface flow is directed poleward in each hemisphere, reaching its peak speed at latitude $L = \pm 6.^\circ 4$ and vanishing at the equator and poles.

In simulating the photospheric field over the interval 1713–1996 (solar cycles −3 through 22), we continue to employ the Snodgrass formula for the photospheric differential rotation, fix the turbulent diffusion rate at $\kappa = 500$ km^2 s^{-1}, and assume a latitudinal profile for the poleward flow given by equation (2). However, the flow amplitude v_m is treated as a free parameter that may vary from one cycle to the next. After the source term and the initial photospheric flux distribution are specified, equation (1) is integrated numerically on a grid of dimensions 128 cells in longitude by 64 cells in latitude.

In Wang & Sheeley (2003a), we found that the general properties of the large-scale field during cycle 21 could be reproduced by employing a source term consisting of 600 bipolar magnetic regions (BMRs), each having a total flux (including both polarities) of 5×10^{22} Mx and a longitudinal pole separation of 15°. Let us assume that, during any given year Y between 1713 and 1996, the rate of flux emergence in active regions scales as the annual group sunspot number $R_G(Y)$ (as defined by Hoyt & Schatten 1998). Since the total flux in large BMRs during cycle 21 is $\Phi_{\rm BMR}^{(21)} \sim 600 \times (5 \times 10^{22}$ Mx$) \sim 3 \times 10^{25}$ Mx and the aggregate group sunspot number over this 10 yr interval

is $R_{\rm tot}^{(21)} = \sum_{Y=1977}^{1986} R_G(Y) = 831.5$, the amount of active region flux that emerges per unit R_G may be estimated as

$$k_G = \frac{\Phi_{\rm BMR}^{(21)}}{R_{\rm tot}^{(21)}} \sim 3.6\times10^{22}\ {\rm Mx}. \quad (3)$$

The total flux emerging during any given year $Y \geq 1713$ is thus taken to be

$$\Phi_{\rm BMR}(Y) = k_G R_G(Y) \sim 3.6\times10^{22}\ {\rm Mx}\ R_G(Y). \quad (4)$$

If we assume that every BMR has a strength of 5×10^{22} Mx, the number of active regions emerging during year Y is

$$N_{\rm BMR}(Y) = \frac{\Phi_{\rm BMR}(Y)}{5\times10^{22}{\rm Mx}} = \left(\frac{600}{R_{\rm tot}^{(21)}}\right) R_G(Y) \sim 0.72 R_G(Y). \quad (5)$$

This form of the source term, in which the number but not the strength of the BMRs varies from cycle to cycle, is designated as $S = S_1$. Alternatively, let us suppose that 600 active regions emerge during every cycle but that their strength scales as $(5\times10^{22}\ {\rm Mx})(R_{\rm tot}^{(n)}/R_{\rm tot}^{(21)})$, where $R_{\rm tot}^{(n)}$ denotes the sum of the yearly group sunspot numbers for cycle n. In that case,

$$N_{\rm BMR}(Y) = \frac{\Phi_{\rm BMR}(Y)}{(5\times10^{22}\ {\rm Mx})\left(R_{\rm tot}^{(n)}/R_{\rm tot}^{(21)}\right)} = \left(\frac{600}{R_{\rm tot}^{(n)}}\right) R_G(Y). \quad (6)$$

This form of the source term, in which the strength but not the number of BMRs varies from cycle to cycle, is designated as $S = S_2$. In both cases, the BMRs are assigned a longitudinal pole separation of 15° and an axial tilt γ relative to the east-west line given by $\sin\gamma = 0.6 \sin|L|$ (see Wang & Sheeley 1991). In accordance with the usual Hale-Joy laws, the east-west polarity orientations of the BMRs are reversed after the minimum of each cycle, with the westward or leading pole being located equatorward of the trailing pole and having the same sign as the initial polar field in that hemisphere. The bipoles are distributed randomly over a 10° wide band centered about a mean latitude L_0, which migrates equatorward according to

$$|L_0(\Delta t)| = 25\overset{\circ}{.}0 - 3\overset{\circ}{.}0(\Delta t) + 0\overset{\circ}{.}13(\Delta t)^2 \quad (7)$$

(based on Fig. 2 of Hathaway et al. 2003), where Δt is the time in years since the start of the given cycle. A random number generator is also used to assign a longitude and a hemisphere (north or south) to each bipole. Although the number of BMRs deposited varies from year to year according to equation (5) or (6), the deposition times are distributed uniformly over each year.

Because their emergence rate is not well constrained and because their characteristic size ($\sim10^4$ km) is below our grid cell resolution, ephemeral regions are not included in our numerical simulations. The contribution of these small bipoles to the total photospheric flux and to the Sun's net dipole moment is considered analytically in § 4.

We extrapolate the photospheric field into the corona by assuming that the current-free condition $\nabla \times \boldsymbol{B} = 0$ holds out to a "source surface" at $r = R_{\rm ss}$, where $B_L = B_\phi = 0$ (see Schatten et al. 1969). As illustrated in Figure 2 of Wang et al. (1996), setting $R_{\rm ss} = 2.5\ R_\odot$ reproduces the global configuration of He I 1083.0 nm coronal holes through both the minimum and maximum phases of the sunspot cycle. Because it is relatively insensitive to the amount of activity present, we fix the source surface radius at 2.5 $R_\odot$ throughout our long-term simulations. The total open flux $\Phi_{\rm open}$ is given by

$$\Phi_{\rm open}(t) = R_{\rm ss}^2 \int |B_r(R_{\rm ss}, L, \phi, t)|\, d\Omega, \quad (8)$$

where the integral is over all solid angles Ω. Since the open flux is distributed isotropically at 1 AU according to *Ulysses* magnetometer observations (Balogh et al. 1995; Smith et al. 2001), the radial field strength at Earth ($r = r_{\rm E}$) is related to $\Phi_{\rm open}$ by

$$B_{\rm E}(t) = \frac{\Phi_{\rm open}(t)}{4\pi r_{\rm E}^2}. \quad (9)$$

Because of the rapid falloff of higher order multipoles between $r = R_\odot$ and $r = R_{\rm ss}$, the main contribution to $\Phi_{\rm open}$ and $B_{\rm E}$ comes from the dipole and (near sunspot maximum) the quadrupole component of the photospheric field.

3. FLUX TRANSPORT SIMULATIONS

We integrate the flux transport equation over 26 solar cycles, starting at the end of the Maunder minimum with cycle −3. Table 1 lists the minimum-to-minimum dates of each cycle, its approximate length in years, its maximum yearly group sunspot number $R_{\rm max}$, and the sum $R_{\rm tot}$ of its yearly group sunspot numbers. To characterize the cycle "amplitude" or "strength," we use $R_{\rm tot}$, which measures the total flux that emerges in active regions over a given cycle, rather than $R_{\rm max}$, which specifies the maximum yearly rate at which this flux emerges.

Consistent with our model for the Maunder minimum (Wang & Sheeley 2003b), we take the initial photospheric flux distribution in 1713 to be

$$B_r(R_\odot, L, \phi, 0) = 3\ {\rm G}\sin^7 L. \quad (10)$$

For comparison, the observed photospheric field during the 1976 sunspot minimum had the form $\sim$12 G $\sin^7 L$ (Svalgaard et al. 1978; Wang & Sheeley 1995). The poleward concentration of the flux is a consequence of the surface meridional flow. We have verified that the solution to equation (1) soon loses its "memory" of the exact form of the initial field, being far more sensitive to the source term S and to variations in the flow speed v_m.

3.1. *Model S1: Number of BMRs Scaled according to Cycle Amplitude*

In our first simulation ("model S1" with $S = S_1$), the number of BMRs is taken to vary as $R_{\rm tot}$ but their strengths are fixed at 5×10^{22} Mx. While constraining v_m to remain in the range $\sim$10–20 m s^{-1}, we adjust its value from one cycle to the next so as to stabilize the oscillations of the polar fields. Table 1 shows the flow amplitude assigned to each cycle in this simulation. In general, the flow is required to be faster and the initial polar fields to be relatively strong for cycles with large $R_{\rm tot}$; otherwise, the polar fields at the end of such high-activity cycles would be too strong to be reversed during the next cycle. Conversely, cycles with small $R_{\rm tot}$ tend to have slower flows and weaker initial polar fields.

Figure 1 shows a latitude-time plot of the photospheric field over the entire 284 yr simulation, constructed by longitudinally averaging maps of $B_r(R_\odot, L, \phi, t)$ taken at successive 27.3 day intervals. The quasi-vertical streaks at mid-latitudes represent magnetic flux streaming from the active regions to the poles; these surges (in which the trailing polarity predominates) act to cancel the old-cycle polar fields and establish the new-cycle ones.

TABLE 1
SOLAR CYCLE DATA

Cycle Number	Dates	Cycle Length (yr)	R_{max}	R_{tot}	v_m (model S1) (m s^{-1})	v_m (model S2) (m s^{-1})
−3	1713–1723	11	33.9	134.5	12	12
−2	1724–1733	10	69.7	277.0	14	13
−1	1734–1744	11	57.7	251.8	14	13
0	1745–1755	11	63.2	282.3	14	14
1	1756–1766	11	68.5	359.3	14	15
2	1767–1775	9	98.5	510.7	15	15
3	1776–1784	9	80.8	390.1	13	13
4	1785–1798	14	89.2	594.0	19	20
5	1799–1810	12	51.1	191.7	11	11
6	1811–1823	13	30.8	159.5	13	14
7	1824–1833	10	64.3	341.4	14	14
8	1834–1843	10	109.4	510.1	14	14
9	1844–1856	13	85.8	536.3	20	20
10	1857–1867	11	85.6	462.1	14	14
11	1868–1878	11	96.2	476.9	14	13
12	1879–1889	11	61.7	334.7	14	14
13	1890–1901	12	88.0	480.3	16	16
14	1902–1913	12	61.4	386.5	15	15
15	1914–1923	10	110.1	495.8	15	15
16	1924–1933	10	82.3	464.1	13	14
17	1934–1944	11	120.6	654.1	17	18
18	1945–1954	10	144.9	716.2	15	15
19	1955–1964	10	175.1	873.7	18	17
20	1965–1976	12	108.5	704.3	19	19
21	1977–1986	10	155.7	831.5	17	17
22	1987–1996	10	148.5	775.0	17	17

In Figure 2*a* we plot the long-term variation of the Sun's axial and equatorial dipole strengths, defined as D_{ax} and $D_{eq} = (H_1^2 + H_2^2)^{1/2}$, where

$$D_{ax}(t) = \frac{3}{4\pi}\int B_r(R_\odot, L, \phi, t)\sin L\, d\Omega, \quad (11)$$

$$H_1(t) = \frac{3}{4\pi}\int B_r(R_\odot, L, \phi, t)\cos L\cos\phi\, d\Omega, \quad (12)$$

$$H_2(t) = \frac{3}{4\pi}\int B_r(R_\odot, L, \phi, t)\cos L\sin\phi\, d\Omega. \quad (13)$$

Figure 2*b* shows the evolution of B_N and B_S, representing the average (signed) field poleward of $L = +60^\circ$ and $L = -60^\circ$, respectively. Finally, Figure 2*c* shows the variation of the near-Earth radial IMF strength, B_E, and of the total photospheric flux expressed as a surface-averaged field strength,

$$B_{tot}(t) = \frac{1}{4\pi}\int |B_r(R_\odot, L, \phi, t)|\, d\Omega. \quad (14)$$

All quantities are calculated at intervals of 27.3 days.

As expected, $D_{ax}(t)$ undergoes regular polarity oscillations with an average period of ~22 yr, attaining its maximum amplitude

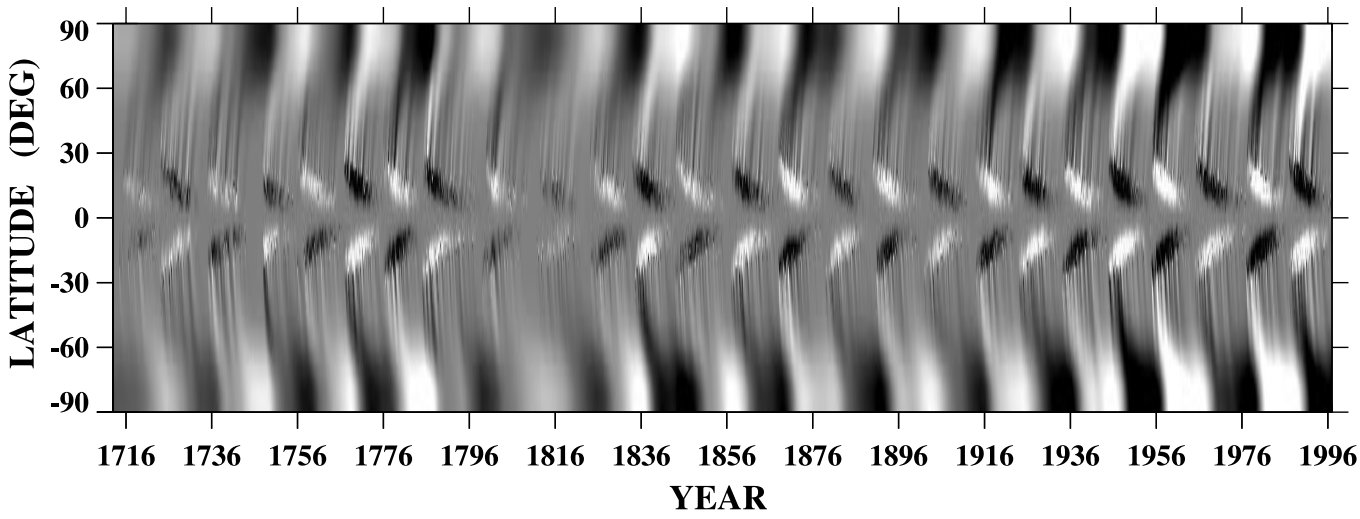

FIG. 1.—Latitude-time plot of the photospheric field over 26 solar cycles (model S1). Each column of pixels represents a 27.3 day Carrington map of the photospheric field averaged over longitude. Gray-scale ranges from $\langle B_r\rangle_\phi < -8$ G (*black*) to $\langle B_r\rangle_\phi > +8$ G (*white*).

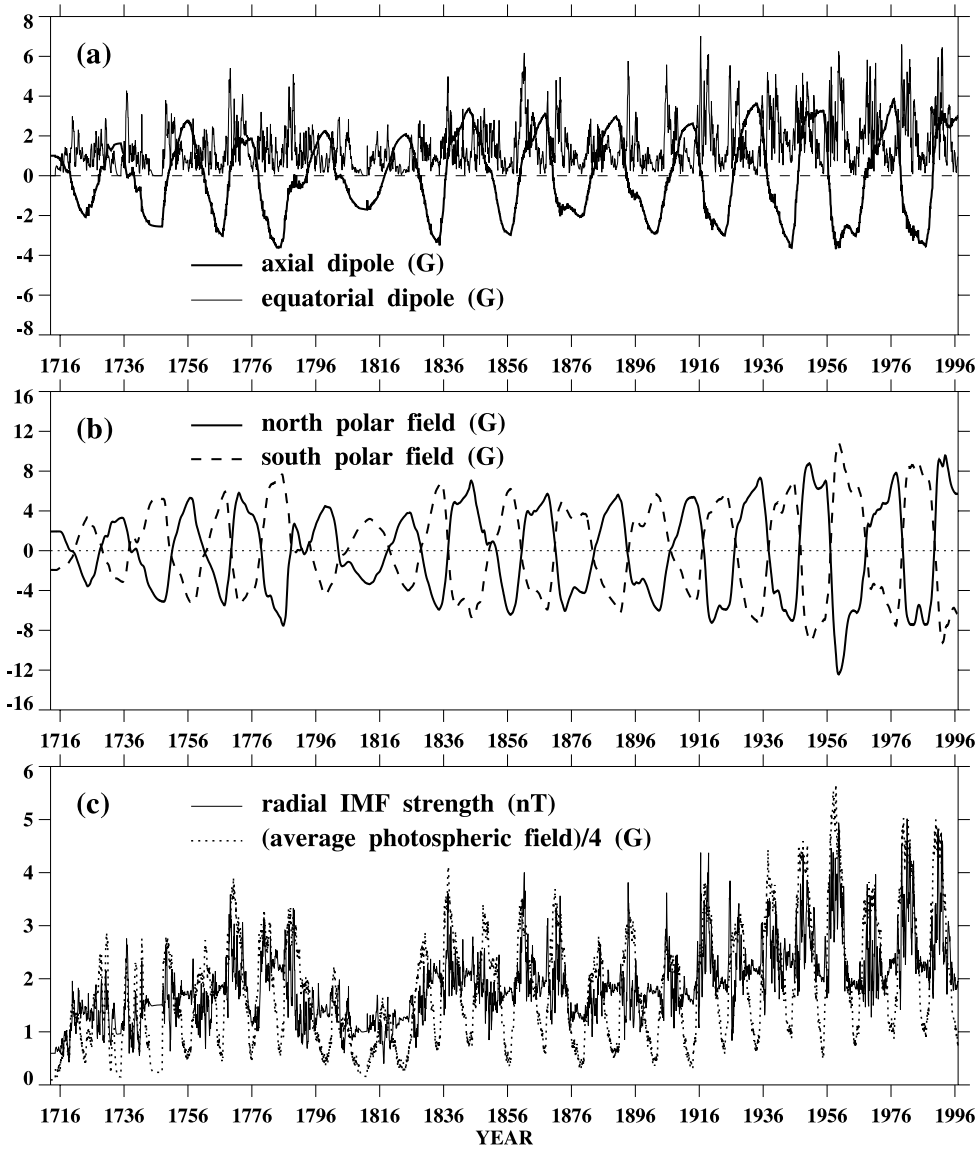

FIG. 2.—Evolution of the large-scale magnetic field over 26 solar cycles (model S1). The BMR sources are all assigned the same strength and are deposited at a rate proportional to the observed yearly sunspot numbers; the poleward flow speed v_m is adjusted from cycle to cycle as indicated in Table 1. (*a*) Variation of the Sun's axial (D_{ax}) and equatorial (D_{eq}) dipole components (G). (*b*) Variation of the north (B_N) and south (B_S) polar fields (G), averaged over 30° polar caps. (*c*) Variation of the near-Earth radial IMF strength B_E (nT) and of the total photospheric flux B_{tot} (expressed as a surface-averaged field strength in units of 4 G).

at sunspot minimum and going through zero near sunspot maximum. In contrast, $D_{eq}(t)$ varies approximately in phase with sunspot activity while undergoing large-amplitude fluctuations on timescales of ~1–2 yr. The smooth, systematic variation of $D_{ax}(t)$ reflects the fact that the north-south dipole moments of the BMRs of a given cycle are aligned in the same sense, so that their resultant grows cumulatively (if latitudinal transport effects are neglected). On the other hand, because the BMRs are deposited at random longitudes, their net equatorial dipole moment undergoes stochastic fluctuations with an amplitude equal to its rms value $\langle D_{eq}^2 \rangle^{1/2}$, which in turn scales as the square root of the BMR emergence rate (Wang & Sheeley 2003a). The width of the peaks is determined by the decay timescale for the equatorial dipole, given by $\tau_{flow} \sim R_\odot / v_m \sim 1.4$ yr (16 m s^{-1}/v_m). The stochastic nature of $D_{eq}(t)$ explains the presence of temporary dips in the IMF strength even at activity maximum (see Fig. 2*c*); such "Gnevyshev gaps" do not require an actual decrease in the flux emergence rate (see Gnevyshev 1967; Storini et al. 1997; Richardson et al. 2000).

From Figures 2*a* and 2*b* we note a tendency for the polarity reversal to occur more suddenly in high-amplitude sunspot cycles than in low-amplitude ones. It is also evident that the variation of $B_N(t)$ and $B_S(t)$ is generally nonmonotonic during any given cycle. In most cases, the polar fields reach their greatest strength at sunspot minimum, with a secondary bump or saddle appearing just after sunspot maximum. However, during some of the shorter, faster rising cycles (including cycles 2, 11, 18, 19, and 22), the main peak occurs ~1–3 yr after sunspot maximum rather than at sunspot minimum. (Both types of behavior may also be seen in the polar faculae counts of Sheeley 1991.) This nonmonotonic variation of the polar fields can be understood as follows. During the rising to early declining phases of each cycle, when BMRs emerge at relatively high latitudes, the meridional flow sweeps copious amounts of flux of both signs to the poles, causing the polar field strength to undergo large fluctuations as the leading-polarity flux partially cancels the trailing-polarity flux that arrives ahead of it. Later in the cycle, when the BMRs are located at low latitudes, more of

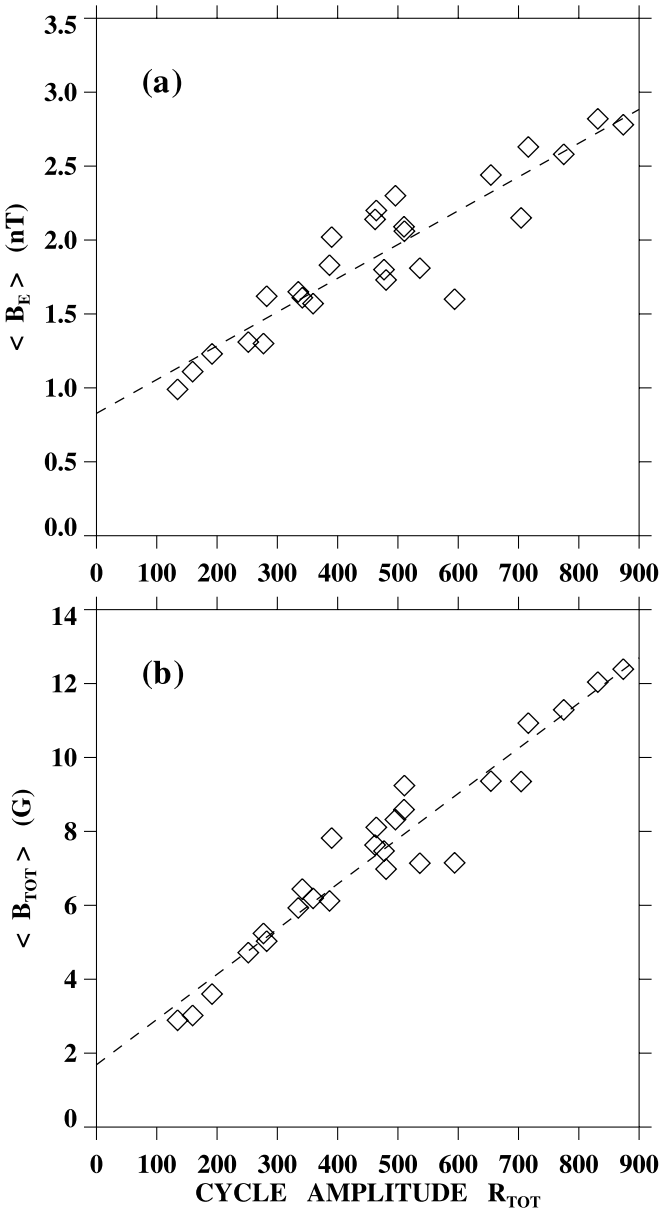

FIG. 3.—Scatter plots of (*a*) cycle-averaged radial IMF strength $\langle B_E \rangle$ (nT) and (*b*) cycle-averaged photospheric flux $\langle B_{tot} \rangle$ (G) against total sunspot number R_{tot} for model S1. In each plot, the leftmost (rightmost) diamond represents solar cycle −3 (19); the diamond lying farthest below the linear least-squares fit (*dashed line*) corresponds to the poorly observed and unusually long cycle 4 (1785–1798).

the leading-polarity flux is able to diffuse across the equator and the relative amount of trailing-polarity flux reaching the poles tends to be greater, resulting in a progressive increase in the polar field strength. Nevertheless, during cycles characterized by steeply rising activity, the polar fields sometimes attain their peak strength not at sunspot minimum but during the earlier, transient phase when the giant surges of alternating polarity arrive at the poles.

From Figure 2*c* we see that the overall secular variation of the open flux tends to track that of the total photospheric flux. Both quantities show a pronounced dip during the Dalton minimum at the beginning of the nineteenth century; they also undergo a progressive increase between cycles 12 and 19. However, on timescales of a solar cycle or less, the behavior of $B_E(t)$ differs considerably from that of $B_{tot}(t)$. In particular, the total photospheric flux varies by a factor of order 5 between sunspot minimum and maximum, whereas the open flux (like the Sun's total dipole strength) varies by a factor of order 2. Moreover, because $D_{eq}(t)$ depends on the longitudinal distribution of the active regions as well as on their emergence rate, the highest peaks in $B_E(t)$ and $B_{tot}(t)$ do not always coincide with each other.

The values of B_{tot} derived for the last six cycle minima range from ∼2 to ∼4 G, with both residual low-latitude activity and the strong polar fields contributing to this surface-averaged field strength. In 1954, when $R_G = 4.4$ and B_{tot} falls to 2 G, the polar fields provide the dominant contribution to the photospheric flux. In this respect, the 1954 activity minimum is similar to the minima of earlier low-amplitude cycles, when our simulations show that the only remaining large-scale field is concentrated at the poles.

Let $\langle B_E \rangle$ and $\langle B_{tot} \rangle$ denote the values of the near-Earth radial IMF strength and the total photospheric flux averaged over each of the 26 solar cycles. Scatter plots of ($\langle B_E \rangle$, R_{tot}) and ($\langle B_{tot} \rangle$, R_{tot}) are displayed in Figure 3, along with the corresponding linear least-squares fits. As the cycle amplitude R_{tot} increases from ∼100 (cycle −3) to ∼900 (cycle 19), $\langle B_E \rangle$ increases from ∼1 to ∼3 nT while $\langle B_{tot} \rangle$ increases from ∼3 to ∼13 G. In our model, both $\langle B_E \rangle$ and $\langle B_{tot} \rangle$ must vanish as $R_{tot} \rightarrow 0$, since polarity reversals require a nonzero source term. However, it is evident that the straight-line fits in Figure 3 do not intersect the origin, with the offset being especially pronounced in the case of the open flux (Fig. 3*a*), where $\langle B_E \rangle \simeq 1$ nT for $R_{tot} = 0$. As shown in Figure 4, a more satisfactory fit may be obtained by assuming that $\langle B_E \rangle$ scales as $R_{tot}^{1/2}$ rather than as R_{tot}. This behavior can be understood by recalling that the variation of $B_E(t)$ is similar to that of the Sun's total dipole strength, $D(t)$. If the BMRs are distributed randomly in longitude and all have the same strength (as in the present simulation), $D_{eq}(t)$ scales as the square root of the number of BMRs that emerge during the lifetime $\sim \tau_{flow}$ of the equatorial dipole (Wang & Sheeley 2003a). Since $\langle B_E \rangle \propto \langle D \rangle \sim \langle D_{eq} \rangle$ and $\langle D_{eq} \rangle \propto R_{tot}^{1/2}$, we conclude that $\langle B_E \rangle$ varies roughly as $R_{tot}^{1/2}$. Unlike the open flux, $B_{tot}(t)$ is determined directly by the strength of the photospheric

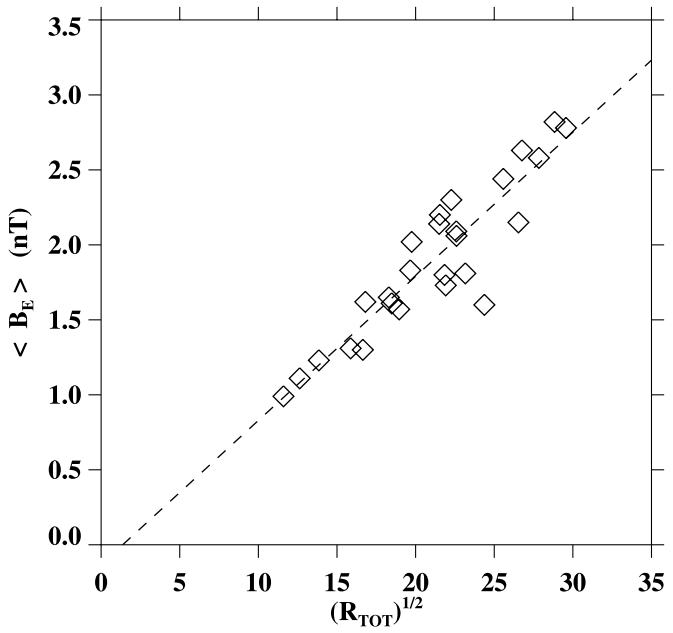

FIG. 4.—Cycle-averaged radial IMF strength $\langle B_E \rangle$ (nT) plotted against $R_{tot}^{1/2}$ (model S1). The dashed line shows a linear least-squares fit to the points. (Compare Fig. 3*a*, where $\langle B_E \rangle$ is plotted against R_{tot} rather than $R_{tot}^{1/2}$.)

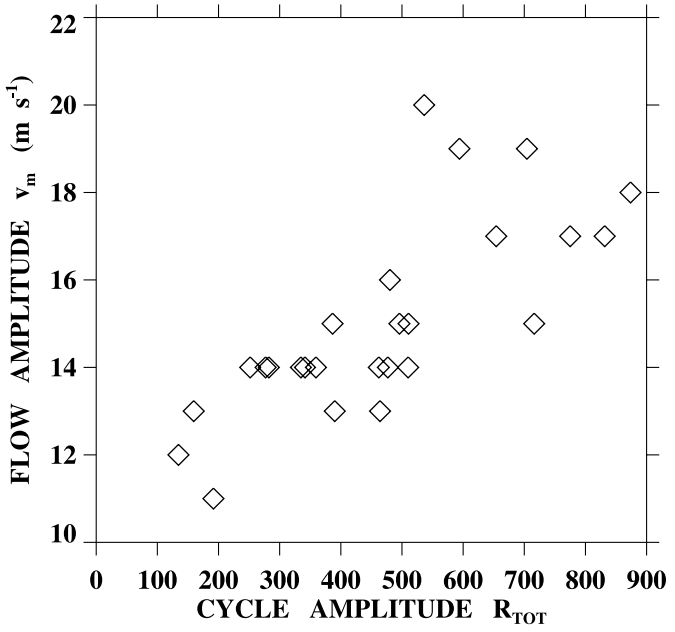

FIG. 5.—Flow amplitude v_m (m s^{-1}) vs. total sunspot number R_{tot} for each of the 26 cycles (model S1).

field at the given time, independent of the locations and axial orientations of the BMRs. However, $\langle B_{tot} \rangle$ grows somewhat more slowly than R_{tot} because the rate of diffusive annihilation increases as the BMRs become more crowded together (see Wang & Sheeley 2003a).

In Figure 5 the poleward flow amplitude v_m is plotted against R_{tot}. In general, the flow was made slower (faster) during less (more) active cycles in order to prevent the final polar fields from becoming overly weak (strong). However, the fastest flows were assigned not to the highest amplitude cycles (19, 21, and 22), but to those characterized by a combination of moderately high amplitudes and long periods (cycles 4, 9, and 20). Because BMRs continue to emerge at low latitudes throughout the extended declining phases of these cycles, the polar fields eventually become too strong to be reversed easily during the next cycle unless the diffusion of leading-polarity flux across the equator is impeded by increasing v_m to $\sim$20 m s^{-1}. When such cycles are included, we find no systematic relationship between flow amplitude and cycle length over the interval 1713–1996 (compare the kinematic dynamo model of Dikpati & Charbonneau 1999, in which the cycle period is inversely proportional to the meridional flow speed).

Figure 6*a* shows a scatter plot of $B_{pol}^{(0)}$ versus R_{tot}, where $B_{pol}^{(0)} \equiv (|B_N^{(0)}| + |B_S^{(0)}|)/2$ represents the polar field strength (averaged between the two hemispheres) at the start of each cycle. There is a clear tendency for $B_{pol}^{(0)}$ to increase as the cycle amplitude increases; this correlation reflects the fact that, in our model, the level of activity during a given cycle must be high enough to reverse the initial polar field. However, the wide scatter about the average trend suggests that $B_{pol}^{(0)}$ can serve only as a rough predictor of cycle amplitude (see Schatten et al. 1978, 1996). As indicated in Figure 6*b*, R_{tot} is also positively correlated with $B_{pol}^{(1)}$, the polar field strength at the end of the cycle. The latter correlation arises because the polar fields at sunspot minimum are formed cumulatively from the active region flux of the past cycle. We note a tendency for both $B_{pol}^{(0)}$ and $B_{pol}^{(1)}$ to level off at high values of R_{tot}, as the faster flows present during the more active cycles carry a greater fraction of

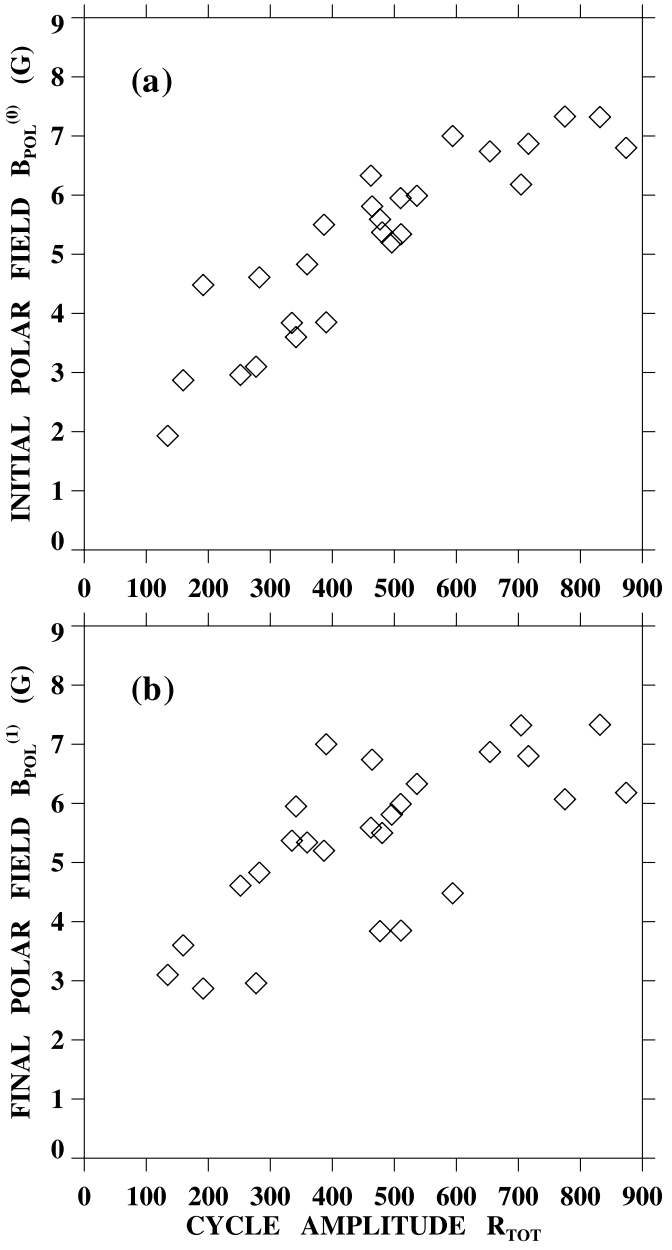

FIG. 6.—Relationship between polar fields and cycle amplitude (model S1). (*a*) Polar field strength at the start of each cycle (averaged between north and south and expressed in G) plotted against total sunspot number R_{tot} for that cycle. (*b*) Polar field strength at the end of each cycle plotted against R_{tot} for that cycle.

the leading-polarity flux to the poles, countering the growth of the polar fields and axial dipole moment.

3.2. *Model S2: BMR Strengths Scaled according to Cycle Amplitude*

In our next simulation ("model S2" with $S = S_2$), the total number of BMRs per cycle is fixed at 600 but their strength varies as the amplitude of the given cycle relative to that of cycle 21. The total flux emerging annually is thus the same as in the previous simulation, but the BMRs are weaker during lower amplitude cycles. We again adjust the values of v_m so as to stabilize the oscillations of the polar fields from one cycle minimum to the next (see Table 1).

Figure 7 shows the evolution of D_{ax}, D_{eq}, B_N, B_S, B_E, and B_{tot} during 1713–1996. In general, the variation of the axisymmetric

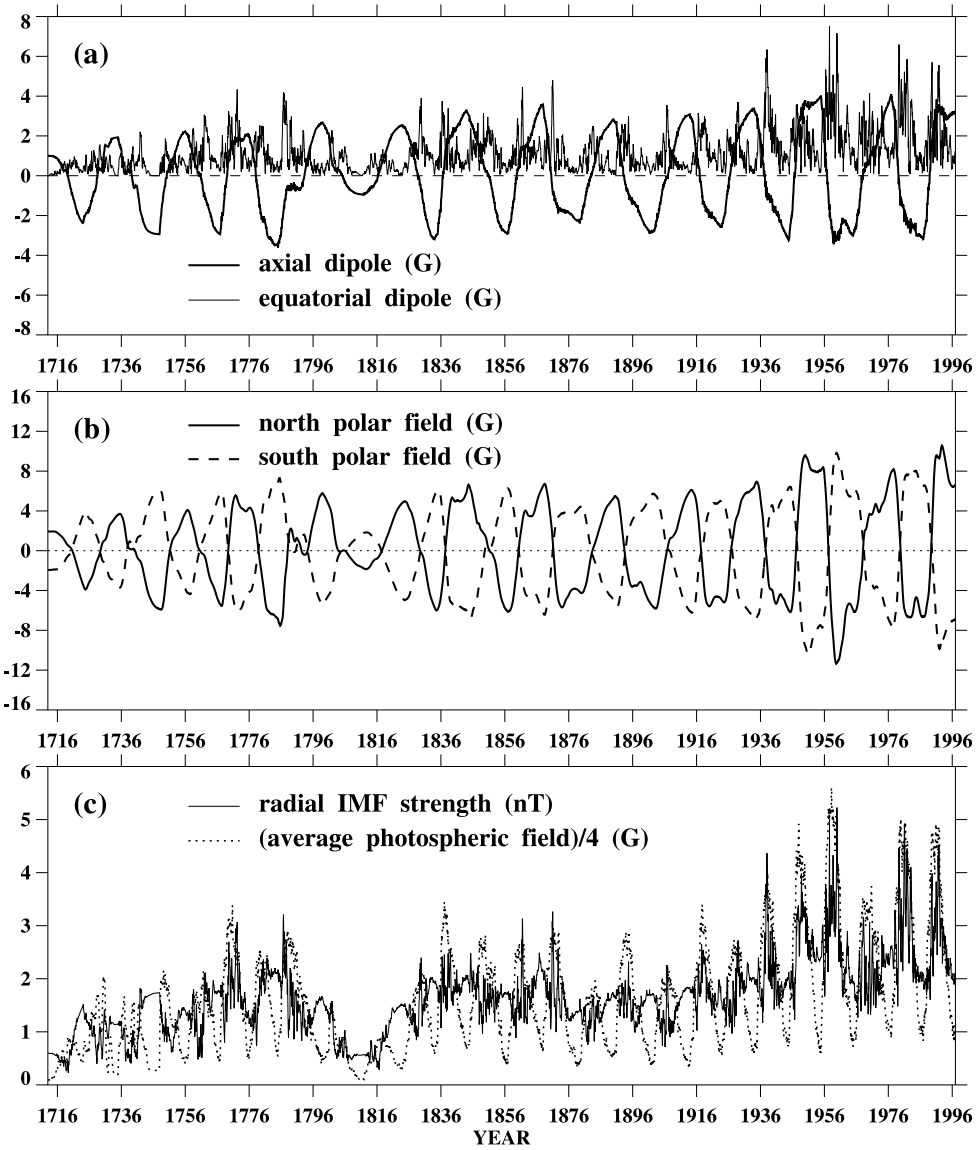

FIG. 7.—Evolution of the large-scale magnetic field over 26 solar cycles (model S2). In this simulation, 600 BMRs are deposited during every cycle while their strengths are scaled according to the cycle amplitude $R_{\rm tot}$; the annual rate of flux emergence is the same as in model S1. The adopted flow speeds are indicated in Table 1. (*a*) $D_{\rm ax}(t)$ and $D_{\rm eq}(t)$. (*b*) $B_N(t)$ and $B_S(t)$. (*c*) $B_{\rm E}(t)$ and $B_{\rm tot}(t)/4$.

field component ($D_{\rm ax}$, B_N, and B_S) resembles that found for model S1 (Fig. 2). However, the long-term behavior of the nonaxisymmetric field component differs significantly from the earlier case. Thus, $D_{\rm eq}$ tends to be weaker during low-amplitude cycles but to increase more rapidly with $R_{\rm tot}$ in the present case (compare Figs. 2*a* and 7*a*); this steeper increase is reflected in the secular evolution of the open flux $B_{\rm E}$ (compare Figs. 2*c* and 7*c*). To interpret this result, we recall that the BMRs are randomly distributed in longitude and that their net equatorial dipole moment therefore scales as the square root of their number times their average strength. In model S1, the BMR strengths are fixed at 5×10^{22} Mx but their number varies as the cycle amplitude, so that $D_{\rm eq}\propto R_{\rm tot}^{1/2}$. In model S2, however, the number of BMRs per cycle is fixed at 600 but their average strength varies as the cycle amplitude, so that $D_{\rm eq}\propto R_{\rm tot}$. The IMF strength thus rises more steeply with activity in the latter model. The same is true for the total photospheric flux $B_{\rm tot}$, which increases linearly with $R_{\rm tot}$ in model S2. In this case, the photospheric field is substantially weaker than in model S1 during the maxima of low-amplitude cycles because the more closely spaced BMRs undergo faster diffusive decay. (Note that the two models are normalized so that their source terms are identical for cycle 21.)

In Figure 8 we display scatter plots of the cycle-averaged $B_{\rm E}$ and $B_{\rm tot}$ versus $R_{\rm tot}$, as derived from model S2. As expected, both $\langle B_{\rm E}\rangle$ and $\langle B_{\rm tot}\rangle$ (like the average BMR strengths) scale approximately linearly with cycle amplitude. Comparing these plots with the corresponding ones for model S1 (Figs. 3*a* and 3*b*), we see that model S2 yields systematically smaller values of $\langle B_{\rm E}\rangle$ and $\langle B_{\rm tot}\rangle$ during low-amplitude cycles.

Figure 9 shows a scatter plot of $\langle D_{\rm eq}\rangle/\langle|D_{\rm ax}|\rangle$ against $R_{\rm tot}$ for model S2. It is apparent that the ratio of the cycle-averaged equatorial and axial dipole strengths increases progressively with cycle amplitude, with the equatorial component being significantly weaker than the axial component during low-amplitude cycles. Because $B_{\rm E}$ scales roughly as $|D_{\rm ax}|$ at sunspot minimum and as $D_{\rm eq}$ at sunspot maximum, the IMF strength tends to show a broad dip during the maximum phase of low-amplitude cycles (see Fig. 7*c*). This trend is consistent with long-term ^{10}Be records, which indicate that the cosmic-ray flux

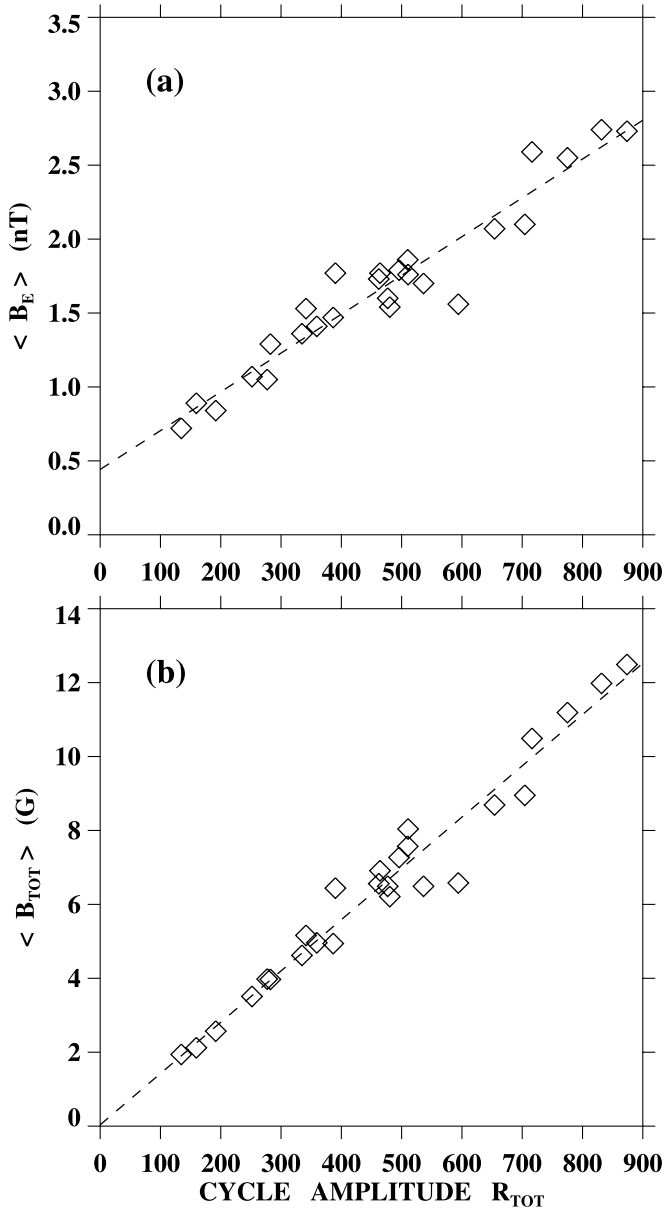

FIG. 8.—Scatter plots of (*a*) cycle-averaged radial IMF strength $\langle B_{\rm E}\rangle$ (nT) and (*b*) cycle-averaged photospheric flux $\langle B_{\rm tot}\rangle$ (G) against total sunspot number $R_{\rm tot}$ for model S2. The dashed line in each plot represents a linear least-squares fit to the 26 data points.

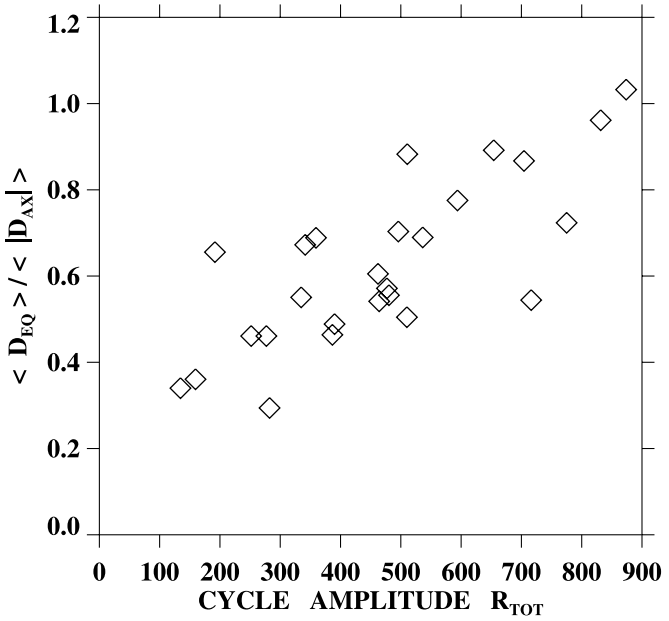

FIG. 9.—Scatter plot of $\langle D_{\rm eq}\rangle/\langle|D_{\rm ax}|\rangle$ vs. $R_{\rm tot}$ (model S2). The cycle-averaged equatorial dipole tends to be significantly weaker than the cycle-averaged axial dipole in low-amplitude cycles.

often peaks at sunspot maximum as well as at sunspot minimum during epochs of low solar activity (McCracken et al. 2002). This systematic weakening of the total dipole moment and IMF strength around the time of polar field reversal should be distinguished from the longitudinal phase effect discussed in § 3.1, whereby fluctuations in the longitudinal distribution of active regions may cause $D_{\rm eq}$ to decrease suddenly even when activity is high. Such stochastic fluctuations produce the relatively narrow, transient dips in $B_{\rm E}$ that occur during both high- and low-amplitude cycles and are seen in both model S1 (Fig. 2*c*) and model S2 (Fig. 7*c*).

4. CONTRIBUTION OF EPHEMERAL REGIONS

Ephemeral regions are small bipoles having pole separations $\Delta s \lesssim 15{,}000$ km, total fluxes $f_0 \sim 10^{19}$ Mx, and lifetimes $\tau <$ 1 day (see Harvey-Angle 1993; Hagenaar 2001; Hagenaar et al. 2003). They are found at all latitudes and have nearly random axial orientations. Estimates of their flux emergence rate over the entire Sun range from $df/dt \sim 3\times10^{22}$ Mx day^{-1} (Harvey-Angle 1993) to as much as $df/dt \sim 5\times10^{23}$ Mx day^{-1} (Hagenaar 2001). According to Harvey-Angle (1993), the emergence rate increases by a factor ~2 between sunspot minimum and maximum; in contrast, Hagenaar et al. (2003) find that ephemeral regions with fluxes $<5\times10^{19}$ Mx show a mild anticorrelation with the solar cycle. In line with the results of Hagenaar et al. (whose sample comprised systematically weaker bipoles than those studied by Harvey-Angle 1993), we assume here that ephemeral regions are distributed uniformly over the solar surface, have random orientations, and emerge at a rate that is roughly constant over the sunspot cycle.

We now use these observed properties together with a simple analytical model to estimate the contribution of ephemeral regions to the total photospheric flux. Consider a succession of small bipoles, each having a total flux f_0, which emerge at average intervals of Δt and at random locations on the solar surface. The rate of flux emergence is then given by $df/dt = f_0/\Delta t$. After each bipole emerges, it decays exponentially on a timescale $\tau \gg \Delta t$. The total flux accumulated after a time $t = n\Delta t$ is

$$F(t) = f_0\left(1 + e^{-\Delta t/\tau} + \cdots + e^{-n\Delta t/\tau}\right) = f_0\left(\frac{1 - e^{-(n+1)\Delta t/\tau}}{1 - e^{-\Delta t/\tau}}\right) \simeq \frac{df}{dt}\tau\left(1 - e^{-(t+\Delta t)/\tau}\right). \quad (15)$$

For $t \gg \tau$, the total flux saturates at a value

$$F_{\rm eph} \simeq \frac{df}{dt}\tau. \quad (16)$$

The contribution of ephemeral regions to the surface-averaged photospheric field may then be expressed as

$$B_{\rm eph} = \frac{F_{\rm eph}}{4\pi R_\odot^2} \simeq 1.6\ {\rm G}\left(\frac{df/dt}{10^{23}\ {\rm Mx\ day^{-1}}}\right)\left(\frac{\tau}{1\ {\rm day}}\right). \quad (17)$$

Thus, if we assume that ephemeral regions emerge at a rate $df/dt \sim 3\times10^{22}$ Mx day^{-1} and decay on a timescale $\tau \sim 1$ day, we obtain $B_{\rm eph} \sim 0.5$ G; if instead we take $df/dt \sim 5\times10^{23}$ Mx day^{-1}, we obtain a much larger equilibrium field strength $B_{\rm eph} \sim 8$ G. The values of $B_{\rm eph}$ are reduced by a factor of 5 if the decay timescale for ephemeral regions is only $\tau \sim 4.4$ hr (Harvey-Angle 1993) instead of $\tau \sim 1$ day.

We may derive a further constraint on $B_{\rm eph}$ from the fact that τ and df/dt are physically coupled: the diffusive decay timescale of the ephemeral regions depends on how closely they are "packed together," which in turn depends on their emergence rate. Let us represent the interacting ephemeral regions by an infinite array of bipoles covering a two-dimensional plane, where each bipole has a pole separation Δs and the mean separation between neighboring bipoles is λ. (The solar surface may be approximated as a flat plane provided $\lambda \ll R_\odot$.) In the absence of new flux emergence, the magnetic field corresponding to this configuration decays exponentially on a timescale

$$\tau \sim \frac{1}{\kappa}\left(\frac{\lambda}{2\pi}\right)^2 \tag{18}$$

(N. R. Sheeley & Y.-M. Wang 2005, in preparation), where κ is the supergranular diffusion constant. Now the total number of ephemeral regions present on the solar surface at any given time is

$$N_{\rm tot} \sim \frac{4\pi R_\odot^2}{\lambda^2}. \tag{19}$$

In the equilibrium state, we also have that

$$N_{\rm tot} \sim \frac{F_{\rm eph}}{f_0} \sim \frac{1}{f_0}\frac{df}{dt}\tau \tag{20}$$

(see eq. [16]). Combining equations (18) through (20), we obtain the following expression for the mean spacing λ between ephemeral regions:

$$\frac{\lambda}{\Delta s} \sim \left[\frac{16\pi^3 R_\odot^2 f_0 \kappa}{(\Delta s)^4 (df/dt)}\right]^{1/4} \sim 2.1\left(\frac{15{,}000\ \text{km}}{\Delta s}\right) \times \left(\frac{f_0}{10^{19}\ \text{Mx}}\right)^{1/4}\left(\frac{10^{23}\ \text{Mx day}^{-1}}{df/dt}\right)^{1/4}\left(\frac{\kappa}{500\ \text{km}^2\ \text{s}^{-1}}\right)^{1/4}. \tag{21}$$

The corresponding decay timescale is

$$\tau \sim \left[\frac{R_\odot^2 f_0}{\pi\kappa(df/dt)}\right]^{1/2} \sim 14.3\ \text{hr}\left(\frac{f_0}{10^{19}\ \text{Mx}}\right)^{1/2} \times \left(\frac{10^{23}\ \text{Mx day}^{-1}}{df/dt}\right)^{1/2}\left(\frac{500\ \text{km}^2\ \text{s}^{-1}}{\kappa}\right)^{1/2} \tag{22}$$

and the equilibrium field strength is given by

$$B_{\rm eph} \sim \frac{1}{4\pi R_\odot^2}\frac{df}{dt}\tau \sim \left[\frac{f_0(df/dt)}{16\pi^3 R_\odot^2 \kappa}\right]^{1/2} \sim 1.0\ \text{G}\left(\frac{f_0}{10^{19}\ \text{Mx}}\right)^{1/2}\left(\frac{df/dt}{10^{23}\ \text{Mx day}^{-1}}\right)^{1/2}\left(\frac{500\ \text{km}^2\ \text{s}^{-1}}{\kappa}\right)^{1/2}. \tag{23}$$

Following Harvey-Angle (1993), let us suppose that $df/dt = 3\times10^{22}$ Mx day^{-1} and $f_0 = 3\times10^{19}$ Mx. From the above equations (with κ and Δs fixed, respectively, at 500 km^2 s^{-1} and 15,000 km), we then estimate that $\lambda \simeq 3.8\Delta s \simeq 57{,}000$ km, $\tau \simeq 45$ hr, and $B_{\rm eph} \simeq 0.9$ G. If instead we follow Hagenaar (2001) by taking $df/dt = 5\times10^{23}$ Mx day^{-1} and $f_0 = 1.13\times10^{19}$ Mx, we find that $\lambda \sim 1.5\Delta s \sim 22{,}000$ km, $\tau \simeq 6.8$ hr (roughly consistent with the value of 4.4 hr measured by Harvey-Angle 1993), and $B_{\rm eph} \simeq 2.3$ G. These estimates suggest an upper limit of $\sim$2–3 G on the contribution of ephemeral regions to the surface-averaged photospheric field during recent activity minima.

In general, the rate at which magnetic bipoles are observed to erupt over the solar surface, like the measured value of the total photospheric flux, depends on the spatial resolution of the magnetograms. If more and more flux emerges on smaller and smaller spatial scales, the question arises as to whether $B_{\rm eph}$ has been greatly underestimated because the observed values of df/dt are far too low. However, we now argue that such a "magnetic flux catastrophe" is unlikely to occur. Suppose that the flux emergence rate for small bipoles scales as $df/dt \propto \delta^{-\nu}$, where $\delta \sim |B_r|/|\nabla_\perp B_r|$ and $\nu > 0$. From the diffusion equation, the decay time scales as $\tau \propto \delta^2/\kappa$. Assuming that the diffusion coefficient κ is independent of δ, we deduce that $B_{\rm eph} \propto (df/dt)\tau \propto \delta^{2-\nu}$. Thus, provided that $\nu \le 2$, the total photospheric flux will not increase indefinitely as the spatial scale δ of the field decreases.

Because of their small size and nearly random orientations, the contribution of ephemeral regions to the Sun's net dipole moment is likely to be negligible. The dipole strength of a single bipole having total flux f_0 and linear pole separation Δs may be expressed as

$$d_0 = \frac{3}{8\pi}\left(\frac{f_0\Delta s}{R_\odot^3}\right) = 5.3\times10^{-6}\ \text{G}\left(\frac{f_0}{10^{19}\ \text{Mx}}\right)\left(\frac{\Delta s}{15{,}000\ \text{km}}\right) \tag{24}$$

(see Wang & Sheeley 1991). If ephemeral regions have random axial orientations and emerge at random locations on the solar surface, the mean-square value of their net dipole strength grows at a rate

$$\frac{d\langle D_{\rm eph}^2\rangle}{dt} \simeq \left(\frac{dN_{\rm eph}}{dt}\right)d_0^2 \simeq \left(\frac{1}{f_0}\frac{df}{dt}\right)d_0^2, \tag{25}$$

where we have omitted dissipation effects due to flux transport. If we also neglect variations in the flux emergence rate df/dt, the cumulative rms dipole strength over an entire solar cycle is then of order

$$\langle D_{\rm eph}^2(\tau_{\rm cyc})\rangle^{1/2} \simeq 3.4\times10^{-2}\ \text{G}\left(\frac{f_0}{10^{19}\ \text{Mx}}\right)^{1/2} \times \left(\frac{df/dt}{10^{23}\ \text{Mx day}^{-1}}\right)^{1/2}\left(\frac{\Delta s}{15{,}000\ \text{km}}\right)\left(\frac{\tau_{\rm cyc}}{11\ \text{yr}}\right)^{1/2}. \tag{26}$$

The inclusion of transport processes will lead to even smaller values of $\langle D_{\rm eph}^2(\tau_{\rm cyc})\rangle^{1/2}$ (see Wang & Sheeley 2003a). For comparison, the contribution of large active regions to the Sun's dipole strength during recent cycles is found to be of order 4 G (see Figs. 2*a* and 7*a*).

From the analysis of this section, we conclude that ephemeral regions have a negligible effect on the Sun's dipole moment and

thus on the IMF strength; however, they may contribute as much as ~2–3 G to the present-day background photospheric field. If the latter contribution is included, the minimum-to-maximum variation in the total photospheric flux during cycle 21 (1977–1986) would be from $B_{\rm tot} \sim 5.5-6.5$ to $B_{\rm tot} \sim 22-23$ G.

Both observationally and theoretically, the secular (cycle-to-cycle) behavior of ephemeral regions and their relation to sunspot activity remain largely unconstrained. In the absence of other evidence, the simplest assumption (and the one that we favor) is that df/dt, f_0, and thus the equilibrium field strength $B_{\rm eph}$, are independent of cycle amplitude. Alternatively, the rate of flux emergence in ephemeral regions might be taken to scale as the total sunspot number in any given cycle ($df/dt \propto R_{\rm tot}$), with the average flux f_0 of an ephemeral region remaining constant; in that case, equation (23) would yield $B_{\rm eph} \propto [f_0(df/dt)]^{1/2} \propto R_{\rm tot}^{1/2}$. A reasonable upper limit on the long-term trend may be obtained by assuming both $f_0 \propto R_{\rm tot}$ and $df/dt \propto R_{\rm tot}$, in which case $B_{\rm eph} \propto R_{\rm tot}$. However, even if the ephemeral region contribution scales linearly with cycle amplitude and is as large as 2–3 G during cycle 21, the net increase in the total photospheric flux $B_{\rm tot}$ between 1713 and 1986 would still be by only ~one-third the amplitude of its variation during cycle 21.

5. COMPARISON WITH GEOMAGNETIC AND COSMOGENIC RECORDS

In Figure 10 we compare the yearly values of $B_{\rm E}$ derived using models S1 and S2 with annual averages of the geomagnetic *aa* index since 1868. The predicted near-Earth radial IMF strength and the *aa* index both exhibit a significant upward trend over the first half of the twentieth century.

According to Lockwood et al. (1999), the power transferred from the solar wind to the Earth's magnetosphere varies as

$$P_w \propto aa \propto n_w^{0.3} v_w^{1.6} B_{\rm E}^{0.8}, \tag{27}$$

where n_w and v_w denote, respectively, the density and velocity of the wind plasma. Empirical studies have shown that the solar wind speed is principally a function of the flux-tube divergence rate near the Sun, rather than of the photospheric or coronal field

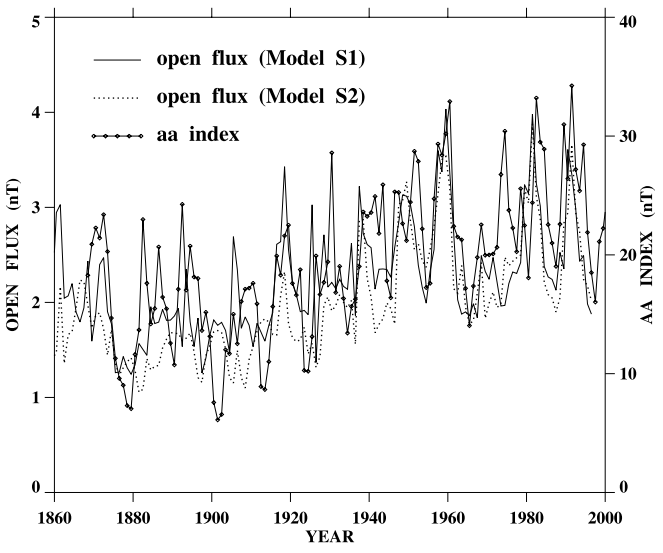

FIG. 10.—Comparison between the simulated open flux and the geomagnetic *aa* index. Yearly values of $B_{\rm E}$ (nT) derived from model S1 (model S2) are indicated by the thin solid (dotted) curve, while annual averages of the *aa* index (nT) are shown as connected diamonds. The vertical axes for $B_{\rm E}$ (*left*) and *aa* (*right*) are related by an arbitrary multiplicative factor of 8.

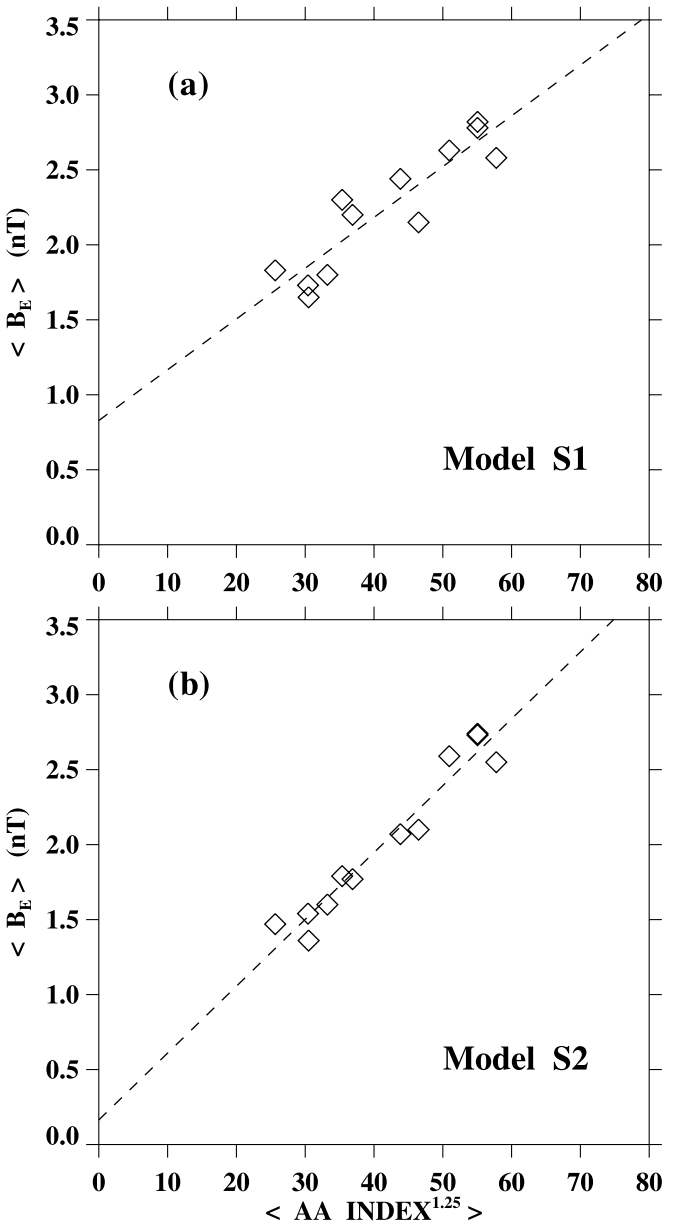

FIG. 11.—Simulated radial IMF strength $\langle B_{\rm E} \rangle$ (nT) vs. $\langle aa^{1.25} \rangle$, where the angle brackets denote cycle averages. (*a*) Model S1. (*b*) Model S2. The dashed line shows a linear least-squares fit to each scatter plot.

strength itself (see Wang & Sheeley 1990; Arge & Pizzo 2000). Since we have no reason to expect a long-term change in the rate of magnetic falloff (areal expansion) inside coronal holes, we assume that the cycle-averaged value of v_w has remained approximately constant since 1868. If we also neglect the relatively weak dependence on the solar wind density, equation (27) implies that

$$\langle B_{\rm E} \rangle \simeq k \langle aa^{1.25} \rangle, \tag{28}$$

where k is a constant and the angle brackets denote cycle averages.

In Figure 11 we display scatter plots of $\langle B_{\rm E} \rangle$ against $\langle aa^{1.25} \rangle$ for cycles 11 through 22, where $\langle B_{\rm E} \rangle$ is derived from model S1 in Figure 11*a* and from model S2 in Figure 11*b*. It is evident that the relationship $\langle B_{\rm E} \rangle \propto \langle aa^{1.25} \rangle$ is approximately satisfied by model S2 but not by model S1, in that the straight-line fit passes close to the origin in the former but not the latter case.

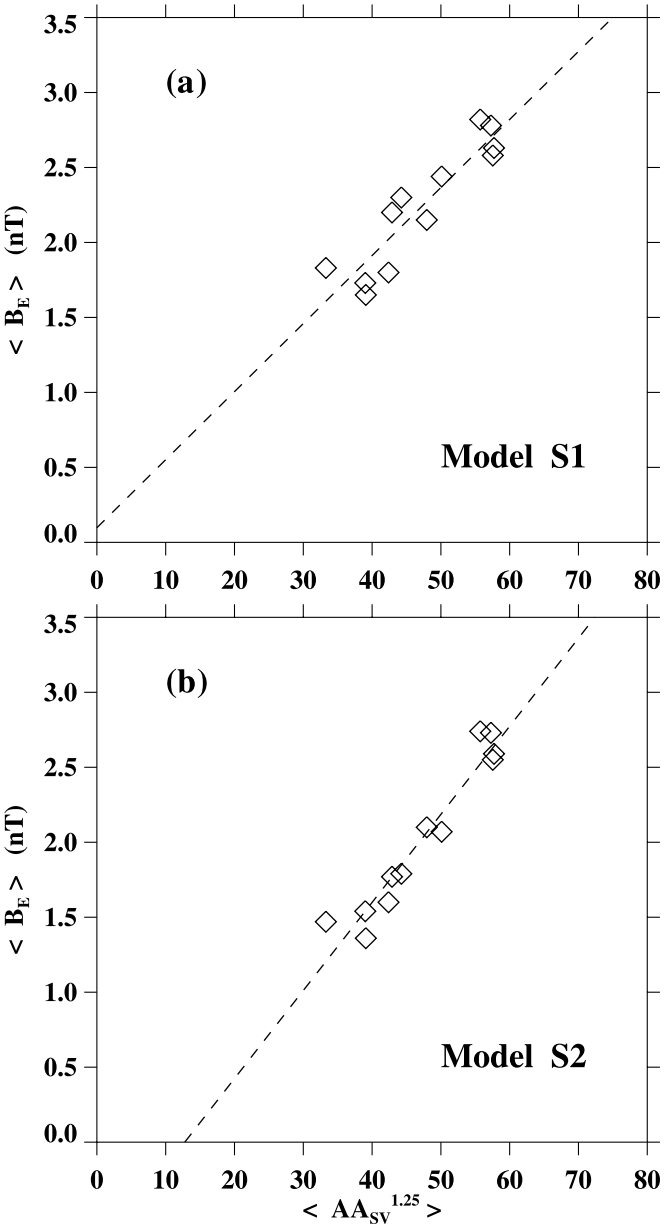

FIG. 12.—Same as in Fig. 11, but with the standard *aa* index replaced by the revised version of Svalgaard et al. (2004).

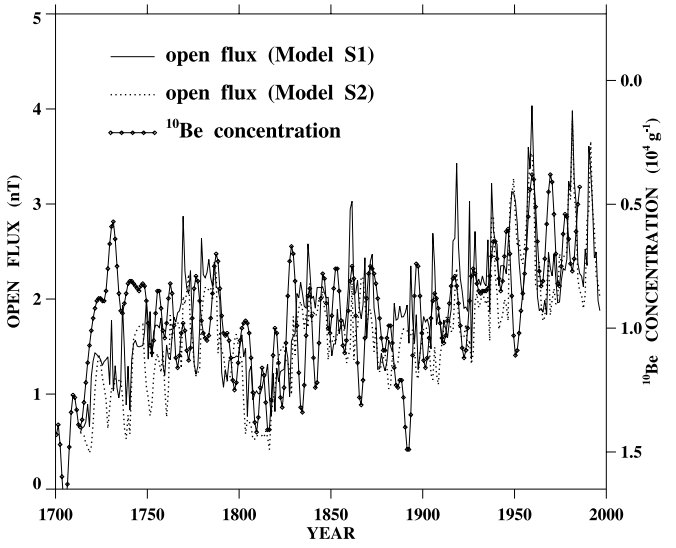

FIG. 13.—Comparison between the simulated open flux and the ^{10}Be cosmogenic isotope record. Yearly values of B_E (nT) derived from model S1 (model S2) are indicated by the thin solid (dotted) curve , while annual ^{10}Be concentrations (in units of 10^4 g^{-1}) are shown as connected diamonds. As discussed in Beer (2000), a low-pass filter has been applied to remove periodicities shorter than 6 yr from the ^{10}Be time series. The relation between the two vertical axes has been arbitrarily adjusted.

Svalgaard et al. (2004) have argued that the standard *aa* index is incorrectly calibrated before 1957 and that it greatly overestimates the secular change in geomagnetic activity. In Figure 12 we plot the values of $\langle B_E \rangle$ derived for each model against $\langle aa_{Sv}^{1.25} \rangle$, where aa_{Sv} denotes the revised *aa* index of Svalgaard et al. We see that it is now model S1 that provides a better fit to the data than model S2. As noted in § 3, $\langle B_E \rangle$ increases roughly as R_{tot} in model S2 but as $R_{tot}^{1/2}$ in model S1; the linear scaling is consistent with the original *aa* time series, whereas the square root dependence accords with the smaller long-term increase in geomagnetic activity found by Svalgaard et al. (2004). Since a more realistic model would allow for variations in both the number and strengths of BMRs, we conjecture that an optimized *aa* index would lie somewhere between the original version and that of Svalgaard et al.

As shown in Wang & Sheeley (2003a), the intracycle fluctuations in the IMF strength depend not just on the amount of activity present (as measured by R_G) but also on the longitudinal distribution of the activity. Because our BMRs have been deposited at random longitudes, the heights and locations of the peaks in $B_E(t)$ are not expected to coincide exactly with the observed ones or with the fluctuations in the *aa* index seen in Figure 10. The effect of different longitude randomizations on the solar cycle evolution of D_{eq} and B_E is illustrated in Figure 5 of Wang & Sheeley (2003a).

The flux of galactic cosmic rays at Earth and hence the production rate of cosmogenic isotopes depend on the cosmic-ray diffusion coefficient, which is usually taken to be inversely proportional to the IMF strength (see Scherer & Fichtner 2004). Figure 13 compares our B_E time series with the variation of the ^{10}Be concentration since 1700. The latter was derived from Greenland ice-core measurements, as described in Beer (2000), and is here plotted on an inverted scale. The secular trend of the simulated open flux tracks that of the ^{10}Be record through most of the 300 yr interval. The largest discrepancy occurs during the period 1720–1750, when sunspot observations were sparse and the R_G yearly means unreliable according to Hoyt & Schatten (1998); the relatively low ^{10}Be concentrations measured at that time suggest that the values of R_{tot} adopted in our simulations (∼250–280: see Table 1) are too low.

6. TOTAL IRRADIANCE VARIATION

Variations in the measured total solar irradiance (TSI) over the solar cycle reflect activity-related variations in the density of bright faculae and dark sunspots covering the solar disk. During cycles 21, 22, and 23, yearly averaged TSI typically showed an ∼0.08% increase (from ∼1365.5 to ∼1366.6 W m^{-2}) between sunspot minimum and maximum, this bolometric change being the net result of a ∼2 W m^{-2} brightening due to faculae and a ∼−1 W m^{-2} darkening due to sunspots (see the review of Fröhlich & Lean 2004). By implication, secular changes in TSI over many solar cycles might be expected to reflect long-term changes in magnetic activity. According to the reconstructions of Lean et al. (1995) and Lean (2000), TSI increased by, respectively, ∼0.19% and ∼0.16% between 1700 and 1986. In

these models, the change in the "quiet-Sun" facular brightness since the Maunder minimum was taken to be comparable to the average difference in Ca II emission between noncycling and cycling Sun-like stars, as inferred by Baliunas & Jastrow (1990). However, the Baliunas & Jastrow results have since been called into question by Hall & Lockwood (2004), who find that the distributions of Ca II H and K core brightness within the cycling and noncycling star populations are essentially the same.

According to the simulations of § 3, $B_{\rm tot}$ varied between ~3.5 and ~20 G during cycle 21 (see Figs. 2*c* and 7*c*). If $B_{\rm tot}$ is regarded as a proxy for the facular brightness, these models would predict that the net increase in the facular background between the Maunder minimum and the end of cycle 21 was by only ~one-fifth of its variation during that cycle. If ephemeral regions are included, the increase would still be by at most ~one-third of the present-day cycle variation. In either case, the secular trend in $B_{\rm tot}$ is significantly smaller than implied by previous irradiance reconstructions, including those of Hoyt & Schatten (1993), Lean et al. (1995), Solanki & Fligge (1999), and Lean (2000), which all require the facular background since 1700 to have increased by an amount comparable to its present minimum-to-maximum variation (see, e.g., Fig. 3 in Lean 2000).

We may obtain a new irradiance reconstruction by following the basic procedure of Lean (2000) but replacing the facular time series shown in Figure 3 of that paper with one that is consistent with the secular trend in $B_{\rm tot}$ found here. The total irradiance may be written as the sum

$$I_{\rm tot} = I_Q + \Delta I_S + \Delta I_{\rm FC} + \Delta I_{\rm FL}, \tag{29}$$

where $I_Q \simeq 1365.5$ W m^{-2} is the lowest measured value of TSI in the contemporary quiet Sun without sunspots, $\Delta I_S < 0$ is the darkening due to the presence of sunspots, $\Delta I_{\rm FC} > 0$ is the intracycle component of the facular brightness variation, and $\Delta I_{\rm FL}$ (which can be of either sign) is the long-term change in facular brightness between cycle minima.

The sunspot darkening component ΔI_S after 1882 is calculated using the semi-empirically determined brightness ratio between sunspots and the quiet photosphere together with observations of sunspot areas and positions (see Lean et al. 1998; Lean 2000). The pre-1882 behavior of ΔI_S is then derived from the yearly group sunspot numbers by assuming

$$\Delta I_S = a_1 R_G + a_2, \tag{30}$$

where the constants a_1 and a_2 are determined by fitting the annual values of ΔI_S after 1882.

The cyclic facular component $\Delta I_{\rm FC}$ for the present-day Sun can be obtained by multiple regression of the measured TSI against ΔI_S and a facular brightening index (the Mg II core-to-wing ratio). The variation of the total facular brightness is assumed to track that of the total photospheric magnetic flux:

$$\Delta I_F \equiv \Delta I_{\rm FC} + \Delta I_{\rm FL} = b_1 B_{\rm tot} + b_2. \tag{31}$$

Here, the constants b_1 and b_2 are determined by regression between annual averages of $B_{\rm tot}$ and $\Delta I_{\rm FC}$ during 1976–1996, when both the simulated photospheric field and the Mg II facular index show little change between cycle minima so that $\Delta I_{\rm FL} \simeq 0$. To justify the simple proportionality assumed in equation (31), we have compared daily values of the facular component of TSI (which includes contributions from both active regions and the background network) with National Solar Observatory/Kitt Peak measurements of the total magnetic flux on the Sun and

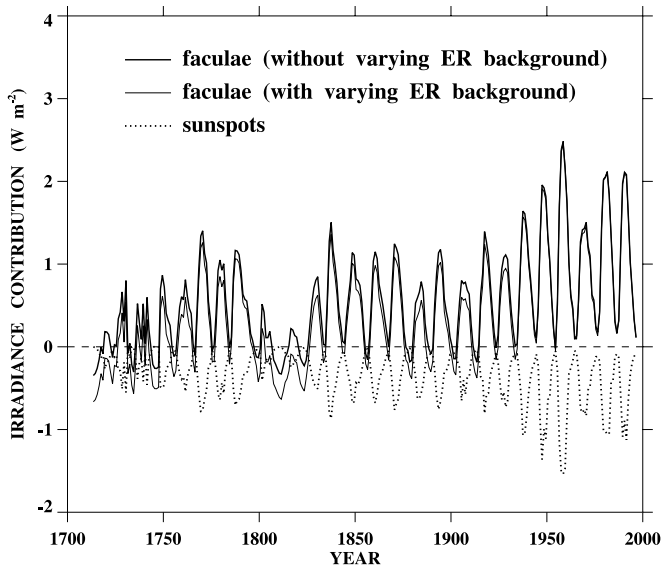

FIG. 14.—Annual variation of the facular brightening (ΔI_F) and sunspot darkening (ΔI_S) contributions to TSI during 1713–1996. The facular component is assumed to track the variation of the total photospheric flux $B_{\rm tot}$, taken here and in the subsequent figures as an average of models S1 and S2; the thick (thin) solid curve shows the resulting $\Delta I_F(t)$ without (with) a secularly varying ephemeral region background.

obtained a correlation coefficient of 0.88 over the interval 1980–2003. In contrast, TSI itself is found to be only weakly correlated (coefficient 0.27) with the observed total photospheric magnetic flux.

Substitution of equations (30) and (31) into equation (29) yields

$$I_{\rm tot} = I_Q + a_1 R_G + a_2 + b_1 B_{\rm tot} + b_2 \tag{32}$$

for the yearly values of TSI since 1713.

We employ two forms of $B_{\rm tot}(t)$: (1) an average of models S1 and S2 without ephemeral regions; and (2) an average of the same models including an ephemeral region background, whose strength during cycle n is given by

$$B_{\rm eph}^{(n)} = 3\ {\rm G}\left(\frac{R_{\rm tot}^{(n)}}{R_{\rm tot}^{(21)}}\right). \tag{33}$$

As discussed at the end of § 4, the latter form of $B_{\rm tot}(t)$ may be regarded as providing an upper limit on the long-term increase in the photospheric magnetic flux (and thus in the solar irradiance). Models S1 and S2 are averaged in this section both for the sake of brevity and because the differences between the secular behavior of $B_{\rm tot}$ in the two cases are relatively small, as a comparison of Figures 3*b* and 8*b* suggests.

Figure 14 shows the annual contributions of faculae (ΔI_F) and sunspots (ΔI_S) to the TSI variation during 1713–1996. It is apparent that the long-term increase of the facular brightness at cycle minimum remains small compared with its present-day solar cycle variation, even when a secularly varying ephemeral region background is included. The resultant yearly values of $I_{\rm tot} = I_Q + \Delta I_S + \Delta I_F$ are displayed in Figure 15. The fractional increase in TSI between 1713 and 1986 is ~0.03% if the varying small-scale background field is absent and ~0.06% if it is present. In either case, the predicted trend is much smaller than the ~0.14% secular increase in TSI obtained by Lean (2000)

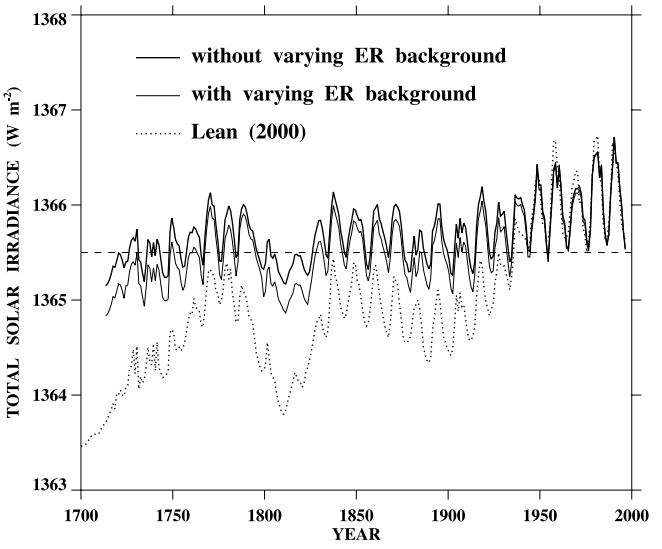

FIG. 15.—Variation of yearly TSI from 1713 to 1996, derived from model (S1+S2)/2 without (*thick solid curve*) and with (*thin solid curve*) a secularly varying ephemeral region background. For comparison, the reconstruction of Lean (2000) is indicated by the dotted curve, while the present-day "quiet-Sun" TSI level ($I_Q = 1365.5$ W m^{-2}) is marked by the dashed line.

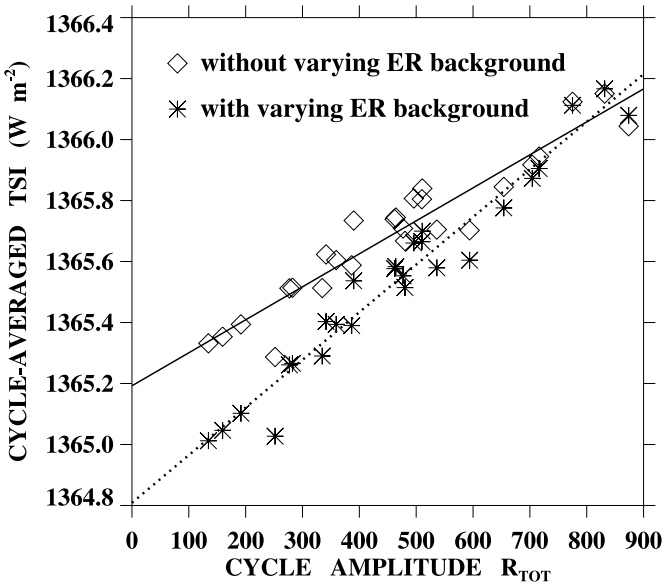

FIG. 16.—Cycle-averaged TSI $\langle I_{tot} \rangle$ plotted against total sunspot number R_{tot}, for model (S1+S2)/2 without (*diamonds*) and with (*asterisks*) a varying small-scale background field. Also shown is a straight-line fit to each case.

over the same period. Our result corresponds to multiplying the long-term facular contribution ΔI_{FL} assumed in the latter paper by a factor of 0.2–0.35.

Although the results are not plotted here, we have also derived the irradiance evolution in three broad spectral bands by scaling down the wavelength-dependent facular background of Lean (2000) to match our new TSI reconstructions. When the ephemeral region component is absent, we find that the irradiance increase between 1713 and 1986 is 0.12% at 112–400 nm, 0.03% at 400–1000 nm, and 0.01% at 10^3–10^5 nm. If a varying small-scale background field is assumed to be present, the corresponding values are 0.19%, 0.05%, and 0.02%. The fractional increase is greatest in the ultraviolet band because the brightness contrast between faculae and the quiet photosphere is greatest at short wavelengths. The changes in total and spectral irradiance between 1713 and 1986 are summarized for the various models in Table 2.

In Figure 16 the cycle-averaged values of I_{tot} are plotted against total sunspot number R_{tot} for each of the 26 cycles. A straight-line fit through the points intersects $R_{tot} = 0$ at $\langle I_{tot} \rangle \simeq 1365.2$ W m^{-2} when the varying ephemeral region background is omitted and at $\langle I_{tot} \rangle \simeq 1364.8$ W m^{-2} when it is included. In either case, the net increase in the cycle-averaged TSI since the Maunder minimum is of order 1 W m^{-2}.

From Figure 15 it is evident that the calculated TSI does not in fact increase linearly with activity when sunspot numbers are high. Thus, we note that the maximum yearly values of I_{tot} for cycle 19 lie somewhat below those for cycles 21 and 22, even though the latter cycles had lower R_G amplitudes. Figure 14 shows that, while the facular brightening component indeed reached its highest level in cycle 19, this peak in ΔI_F was offset by an unusually large sunspot blocking contribution ΔI_S. The relative amplitudes of TSI variation during cycles 19, 21, and 22 depend to some extent on the intercalibration between sunspot area data from different observatories; following Fligge & Solanki (1997), we have reduced the pre-1976 Greenwich sunspot areas by 20%. Although the ordering of the peaks in I_{tot} for these three most active cycles remains somewhat uncertain, there is a clear tendency for TSI to saturate (if not to decrease) when activity is very high. This behavior can be understood on both observational and physical grounds.

Observationally, the area ratio of faculae to sunspots shows a tendency to decrease with increasing sunspot activity (Foukal 1993, 1998; Chapman et al. 1997). Correspondingly, when daily TSI measurements are plotted against the international sunspot number R_I, a quadratic fit has its maximum centered around $R_I \sim 150$ (see Fig. 1 of Solanki & Fligge 1999). We now verify that these empirical results are consistent with our flux transport simulations of the photospheric field.

Figure 17 shows annual averages of the total photospheric flux B_{tot} for 1713–1996 plotted against the yearly group sunspot numbers R_G. It is apparent that B_{tot} initially rises steeply with R_G but subsequently bends over, with the curvature being somewhat more pronounced when the varying ephemeral region background is omitted (Fig. 17*a*) than when it is included (Fig. 17*b*). (Although only the average of the models is shown

TABLE 2

TOTAL AND SPECTRAL IRRADIANCE INCREASES BETWEEN 1713 AND 1986

Wavelength Band (nm)	(S1+S2)/2 Without ER (W m^{-2})	(S1+S2)/2 With ER (W m^{-2})	Lean (2000) (W m^{-2})
Total	0.424 (0.031%)	0.764 (0.056%)	1.941 (0.142%)
112–400	0.126 (0.116%)	0.206 (0.189%)	0.541 (0.499%)
400–1000	0.239 (0.028%)	0.421 (0.050%)	1.185 (0.141%)
10^3–10^5	0.033 (0.008%)	0.066 (0.016%)	0.206 (0.050%)

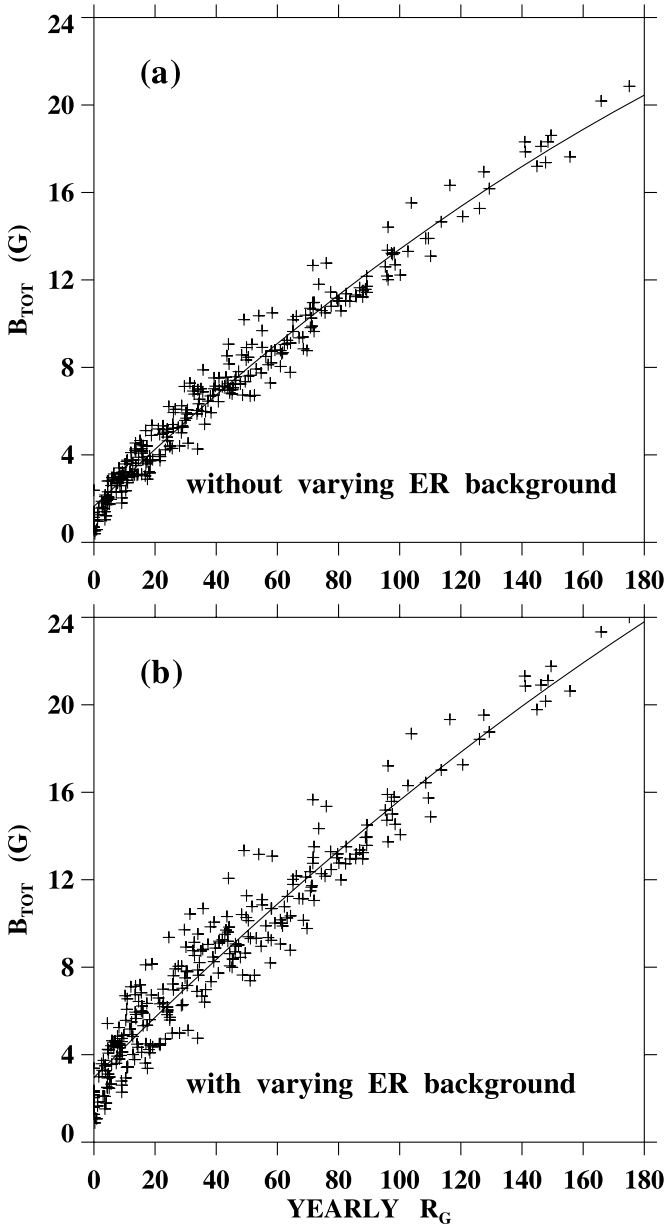

FIG. 17.—Annual averages of $B_{\rm tot}$ for 1713–1996 plotted against yearly group sunspot number R_G, for model (S1+S2)/2 (*a*) without and (*b*) with a varying ephemeral region background. The solid curve represents a quadratic fit to each scatter plot.

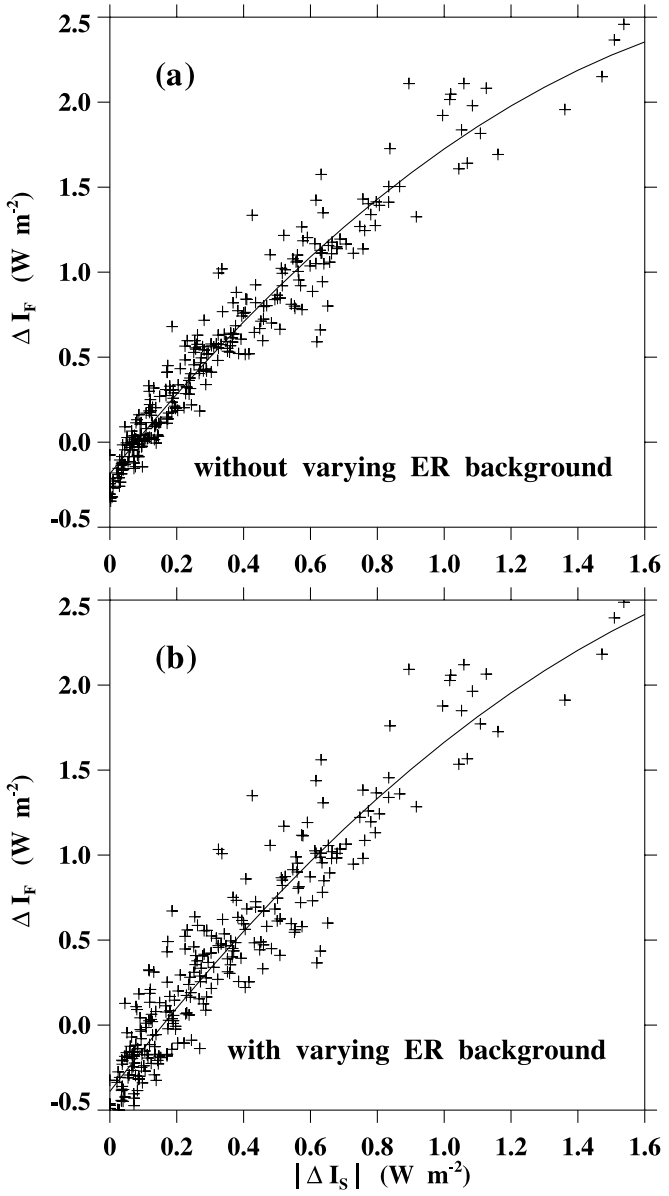

FIG. 18.—Annual averages of facular brightening ΔI_F plotted against sunspot darkening $|\Delta I_S|$, for model (S1+S2)/2 (*a*) without and (*b*) with a varying ephemeral region background. The solid curve represents a quadratic fit to each scatter plot.

here, the curvature is also more pronounced in model S1 than in model S2.) Since the facular brightness is assumed to be proportional to the total photospheric flux, this decrease in the growth rate of $B_{\rm tot}$ is reflected in the corresponding plots of ΔI_F versus $|\Delta I_S|$ displayed in Figure 18.

The nonlinear behavior of $B_{\rm tot}$ seen in Figure 17 is a consequence of diffusive flux transport: as the sunspot number increases, the average spacing between active regions decreases, thereby accelerating the diffusive decay of the active region fields. By analogy with equations (16) and (17) for ephemeral regions, we may write for the total active region flux

$$B_a \propto \frac{df_a}{dt}\tau_a \propto R_G\tau_a, \tag{34}$$

where $df_a/dt \propto R_G$ is the rate at which the flux emerges and τ_a is its decay timescale. If τ_a were a constant independent of R_G, B_a would scale linearly with R_G. However, according to equation (18) (which in turn is based on the diffusion equation), $\tau_a \propto \lambda_a^2$, where λ_a represents the mean separation between active regions. Since λ_a decreases with increasing R_G, it follows that B_a must grow more slowly than R_G. In the presence of diffusion alone (and neglecting any variation in the average strength of active regions), equations (21) through (23) would give $\lambda_a \propto R_G^{-1/4}$, $\tau_a \propto R_G^{-1/2}$, and $B_a \propto R_G^{1/2}$; however, the behavior of the decay timescale will be modified by the presence of differential rotation and meridional flow. We note that the nonlinearity is more pronounced in model S1, where the number of BMRs deposited varies from cycle to cycle, as well as from year to year, than in model S2, where the total number of BMRs per cycle remains fixed. The inclusion of ephemeral regions yields less curvature and more scatter in the $B_{\rm tot}$ versus R_G relationship (compare Fig. 17*b* with Fig. 17*a*) because of our assumption that $B_{\rm eph} \propto R_{\rm tot}$ (eq. [33]). We remark that the results shown in Figure 17 are in general agreement with the

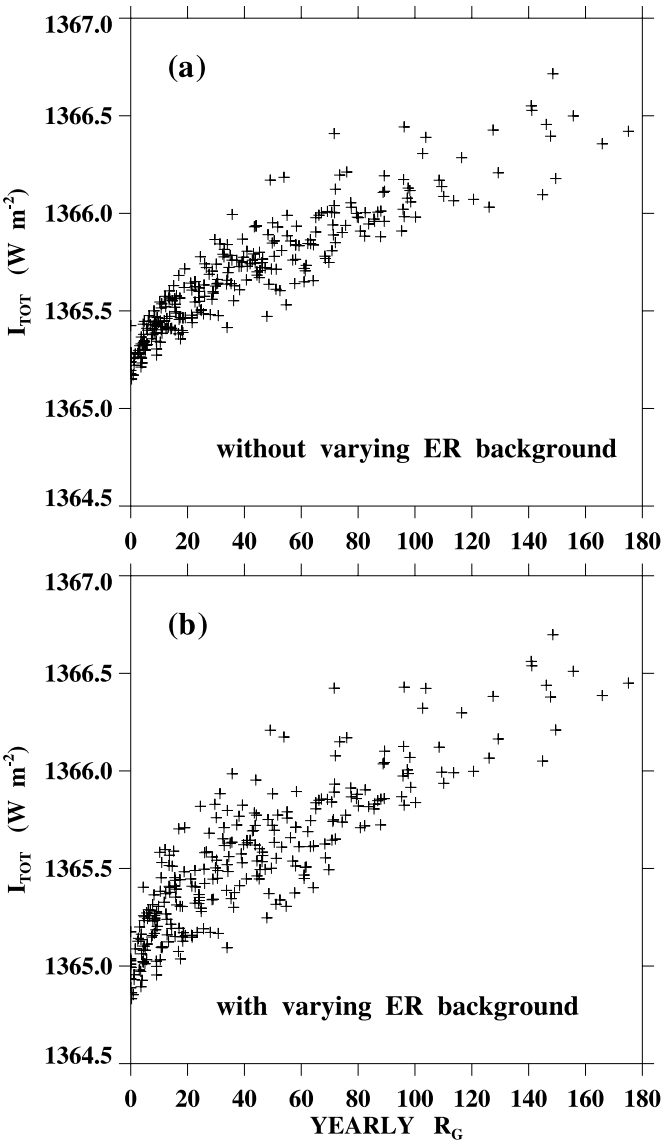

FIG. 19.—Annual averages of TSI for 1713–1996 plotted against R_G, for model (S1+S2)/2 (*a*) without and (*b*) with a varying small-scale background field.

simulations of Schrijver (2001), who found that the relationship between the total photospheric flux and the flux emergence rate obeys a power law with index 0.7 (1.0) if ephemeral regions are omitted (included).

Figure 19 shows the simulated annual values of I_{tot} plotted against R_G, both without and with the varying ephemeral region background. The scatter plots suggest that TSI starts to saturate around $R_G \sim 150$, consistent with Figure 15 and with the daily measurements displayed in Solanki & Fligge (1999). The simulations need to be extended beyond $R_G \sim 180$ in order to verify the presence of the hypothesized downturn.

7. SUMMARY AND DISCUSSION

In this study, we have used a magnetic flux transport model to explore the long-term relationship between sunspot activity, the total photospheric flux, the open flux, and solar irradiance. Our main results may be summarized as follows:

1. The radial IMF strength tends to increase with increasing cycle amplitude, with the rate of increase depending on how the emerging flux is distributed among active regions. If the average strength of the BMRs remains fixed but their number varies as the cycle amplitude R_{tot} ("model S1"), the cycle-averaged IMF strength $\langle B_E \rangle$ scales roughly as $R_{tot}^{1/2}$. However, if the number of BMRs per cycle is fixed but their average strength varies as R_{tot} ("model S2"), then $\langle B_E \rangle$ is roughly proportional to R_{tot}. Since the actual source distribution is likely to be a mixture of these two cases, our simulations suggest that the open flux grows faster than $R_{tot}^{1/2}$ but more slowly than R_{tot}.

2. In model S2, the ratio $\langle D_{eq} \rangle / \langle |D_{ax}| \rangle$ of equatorial to axial dipole strength is substantially less than unity during low-amplitude cycles. As a result, the open flux tends to show a broad dip around the maximum phase of such cycles, consistent with the 5 yr modulation detected in the cosmogenic isotope record by McCracken et al. (2002).

3. Polar field reversals were maintained through all 26 cycles by varying the poleward flow velocity v_m between 11 and 20 m s^{-1}, with the lowest speeds being assigned to the least active cycles. No clear relationship was found between v_m and cycle length.

4. A positive correlation exists between the cycle amplitude and the polar field strength at the start of the cycle (Fig. 6*a*).

5. In the absence of ephemeral regions, the strength of the surface-averaged photospheric field during recent sunspot minima (maxima) is found to be $B_{tot} \sim 3.5$ G ($B_{tot} \sim 20$ G). (Both active region remnants and the strong polar fields contribute to the residual flux at sunspot minimum.) According to either model S1 or S2, the minimum-to-maximum variation of B_{tot} during cycle 21 was $\sim$5 times greater than its secular increase between 1713 and the 1986 sunspot minimum.

6. From the measured rates of ephemeral region emergence and from physical estimates of their decay timescales, we derive an upper limit of $B_{eph} \sim 2-3$ G for the total photospheric flux contributed by ephemeral regions during recent sunspot cycles. If this contribution is included and is scaled according to cycle amplitude, the minimum-to-maximum variation of B_{tot} during cycle 21 is still $\sim$3 times larger than its secular increase between 1713 and 1986.

7. When the simulated $B_{tot}(t)$ is used to reconstruct the long-term facular brightness variation, the increase in TSI between 1713 and 1986 is found to be about one-half of its present-day intracycle variation of $\sim$0.08%. The cycle-averaged increase in TSI since the Maunder minimum is estimated to be $\sim$1 W m^{-2}.

8. The total photospheric magnetic flux grows more slowly than R_G because the diffusive decay rate increases as the active regions become more crowded together. As a result, the derived yearly TSI begins to saturate when $R_G \sim 150$.

Our simulations indicate a significant increase in the cycle-averaged IMF strength since 1880, in general agreement with the deduction of Lockwood et al. (1999) based on the *aa* index. The secular change predicted by model S2 ($\langle B_E \rangle \propto R_{tot}$) is consistent with the standard *aa* time series, whereas model S1 gives a smaller upward trend ($\langle B_E \rangle \propto R_{tot}^{1/2}$) that agrees better with the revised *aa* index of Svalgaard et al. (2004).

Our reconstruction of the total photospheric flux yields a substantially smaller secular trend than predicted by Solanki et al. (2002). This difference arises mainly because, in the model of Solanki et al., the contribution of ephemeral regions to the photospheric field during recent cycle minima is taken to be as high as $B_{eph} \sim 8$ G; in contrast, we find that $B_{eph} < 3$ G from a physical constraint relating the decay timescale of ephemeral regions to their emergence rate.

The models presented here could be improved by adopting more realistic source terms to describe the emergence of active

region flux. Rather than assigning the same strength and longitudinal pole separation to every BMR, we plan in subsequent work to employ an observationally based distribution of sizes, as in the simulations of Schrijver (2001) or of Wang et al. (2002b), where the source term comprised 3000 bipoles whose properties were determined individually from magnetograms taken during cycle 21 (see Wang & Sheeley 1989). The evolution of the large-scale field is sensitive not only to the meridional flow speed but also to the latitudes of emergence and axial tilts of the active regions; these parameters can be more tightly constrained using historical sunspot records.

This study of the long-term behavior of the Sun's magnetic field and irradiance also points to the need for a better understanding of the sources of the background field and irradiance during recent cycle minima. The origin of ephemeral regions and their relation to the sunspot cycle and to the mechanisms that generate active region fields remain to be clarified. Observationally, it has yet to be established that this small-scale component becomes weaker during lower amplitude cycles, as assumed in some of the long-term reconstructions.

We are indebted to M. Lockwood and L. Svalgaard for discussions and for providing their respective versions of the *aa* index; we also thank the referee for comments. This work was supported by NASA and the Office of Naval Research.

REFERENCES

Arge, C. N., & Pizzo, V. J. 2000, J. Geophys. Res., 105, 10465
Baliunas, S., & Jastrow, R. 1990, Nature, 348, 520
Balogh, A., Smith, E. J., Tsurutani, B. T., Southwood, D. J., Forsyth, R. J., & Horbury, T. S. 1995, Science, 268, 1007
Beer, J. 2000, Space Sci. Rev., 94, 53
Cane, H. V., Wibberenz, G., Richardson, I. G., & von Rosenvinge, T. T. 1999, Geophys. Res. Lett., 26, 565
Chapman, G. A., Cookson, A. M., & Dobias, J. J. 1997, ApJ, 482, 541
Dikpati, M., & Charbonneau, P. 1999, ApJ, 518, 508
Eddy, J. A. 1976, Science, 192, 1189
Fligge, M., & Solanki, S. K. 1997, Sol. Phys., 173, 427
Foukal, P. 1993, Sol. Phys., 148, 219
———. 1998, ApJ, 500, 958
Foukal, P., & Lean, J. 1988, ApJ, 328, 347
Fröhlich, C., & Lean, J. 2004, A&A Rev., 12, 273
Gnevyshev, M. N. 1967, Sol. Phys., 1, 107
Hagenaar, H. J. 2001, ApJ, 555, 448
Hagenaar, H. J., Schrijver, C. J., & Title, A. M. 2003, ApJ, 584, 1107
Hall, J. C., & Lockwood, G. W. 2004, ApJ, 614, 942
Harvey, K. L. 1994, in Solar Surface Magnetism, ed. R. J. Rutten & C. J. Schrijver (Dordrecht: Kluwer), 347
Harvey-Angle, K. L. 1993, Ph.D. thesis, Univ. Utrecht
Hathaway, D. H., Nandy, D., Wilson, R. M., & Reichmann, E. J. 2003, ApJ, 589, 665
Howard, R. F. 1989, Sol. Phys., 123, 271
Hoyt, D. V., & Schatten, K. H. 1993, J. Geophys. Res., 98, 18895
———. 1996, Sol. Phys., 165, 181
———. 1998, Sol. Phys., 181, 491
Lean, J. 2000, Geophys. Res. Lett., 27, 2425
Lean, J., Beer, J., & Bradley, R. 1995, Geophys. Res. Lett., 22, 3195
Lean, J. L., Cook, J., Marquette, W., & Johannesson, A. 1998, ApJ, 492, 390
Lean, J. L., Wang, Y.-M., & Sheeley, N. R., Jr. 2002, Geophys. Res. Lett., 29(24), 77
Leighton, R. B. 1964, ApJ, 140, 1547
Lockwood, M. 2001, J. Geophys. Res., 106, 16021
Lockwood, M., Stamper, R., & Wild, M. N. 1999, Nature, 399, 437
McCracken, K. G., Beer, J., & McDonald, F. B. 2002, Geophys. Res. Lett., 29(24), 14
Richardson, I. G., Cliver, E. W., & Cane, H. V. 2000, J. Geophys. Res., 105, 18203
Schatten, K., Myers, D. J., & Sofia, S. 1996, Geophys. Res. Lett., 23, 605
Schatten, K. H., Scherrer, P. H., Svalgaard, L., & Wilcox, J. M. 1978, Geophys. Res. Lett., 5, 411
Schatten, K. H., Wilcox, J. M., & Ness, N. F. 1969, Sol. Phys., 6, 442
Scherer, K., & Fichtner, H. 2004, A&A, 413, L11
Schrijver, C. J. 2001, ApJ, 547, 475
Schrijver, C. J., DeRosa, M. L., & Title, A. M. 2002, ApJ, 577, 1006
Schrijver, C. J., et al. 1998, Nature, 394, 152
Sheeley, N. R., Jr. 1991, ApJ, 374, 386
Sheeley, N. R., Jr., DeVore, C. R., & Boris, J. P. 1985, Sol. Phys., 98, 219
Smith, E. J., Balogh, A., Forsyth, R. J., & McComas, D. J. 2001, Geophys. Res. Lett., 28, 4159
Snodgrass, H. B. 1983, ApJ, 270, 288
Solanki, S. K., & Fligge, M. 1999, Geophys. Res. Lett., 26, 2465
Solanki, S. K., Schüssler, M., & Fligge, M. 2002, A&A, 383, 706
Storini, M., Pase, S., Sýkora, J., & Parisi, M. 1997, Sol. Phys., 172, 317
Svalgaard, L., Cliver, E. W., & Le Sager, P. 2004, Adv. Space Res., 34(2), 436
Svalgaard, L., Duvall, T. L., Jr., & Scherrer, P. H. 1978, Sol. Phys., 58, 225
Wang, Y.-M., Hawley, S. H., & Sheeley, N. R., Jr. 1996, Science, 271, 464
Wang, Y.-M., Lean, J., & Sheeley, N. R., Jr. 2000, Geophys. Res. Lett., 27, 505
———. 2002a, ApJ, 577, L53
Wang, Y.-M., & Sheeley, N. R., Jr. 1989, Sol. Phys., 124, 81
———. 1990, ApJ, 355, 726
———. 1991, ApJ, 375, 761
———. 1995, ApJ, 447, L143
———. 2003a, ApJ, 590, 1111
———. 2003b, ApJ, 591, 1248
Wang, Y.-M., Sheeley, N. R., Jr., & Lean, J. 2002b, ApJ, 580, 1188